

Title: Corrosion resistance and microstructural stability of austenitic Fe-Cr-Al-Ni model alloys exposed to oxygen-containing molten lead

Authors: Hao Shi^a, Adrian Jianu^a, Alfons Weisenburger^a, Chongchong Tang^b, Annette Heinzl^a, Renate Fetzner^a, Fabian Lang^a, Robert Stieglitz^c, Georg Müller^a

^a Institute for Pulsed Power and Microwave Technology, Karlsruhe Institute of Technology (KIT), Hermann- von-Helmholtz-Platz 1, 76344 Eggenstein-Leopoldshafen, Germany

^b Institute for Applied Materials (IAM), Karlsruhe Institute of Technology (KIT), Hermann- von-Helmholtz-Platz 1, 76344 Eggenstein-Leopoldshafen, Germany

^c Institute for Neutron for Neutron Physics and Reactor Technology, Karlsruhe Institute of Technology (KIT), Hermann- von-Helmholtz-Platz 1, 76344 Eggenstein-Leopoldshafen, Germany

Keywords: Fe-Cr-Al-Ni alloy; Molten-Pb; Selective oxidation; Alumina-forming austenitic alloys; Corrosion resistance.

Abstract

The goal of the study was to determine the critical concentrations of Al, Cr and Ni, at which the quaternary Fe-Cr-Al-Ni model alloys, exposed to oxygen-containing molten Pb up to 600°C, are corrosion resistant, while preserving the austenite structure of the alloy matrix.

Twelve alloys were designed to meet the above mentioned requirements; six of them showed corrosion resistance and preserved the austenite phase in the alloy bulk, during the exposure at 550°C and 600°C for 1000 hours to molten Pb containing 10⁻⁶ wt.% oxygen. Based on experimental results a general formula was substantiated as follows: Fe-(20-29)Ni-(15.2-16.5)Cr-(2.3-4.3)Al (wt.%). In case of temperatures below 550°C, the critical Cr content was 14.4 wt.%.

Two corundum-type crystalline structures were identified as the constituent phases of the passivating scales, one being Cr₂O₃ and the other Al₂O₃-Cr₂O₃ solid solution. The average amount of Cr₂O₃ in the Al₂O₃-Cr₂O₃ solid solution, found in the passivating scales of the Fe-Cr-Al-Ni model alloys, was estimated at ≈ 40 wt.% at 550°C and ≈ 35 wt.% at 600°C.

A transitional layer, consisting of Fe- and Ni-enriched austenitic matrix and exhibiting randomly distributed intermetallic B₂-(Ni,Fe)Al, was formed below the oxide scale up to a depth of two microns.

The austenite, as matrix, and Ni₃(Al,Fe) as precipitates are the microstructural phases of the bulk alloys after exposure for 1000h at 600°C to oxygen-containing molten Pb.

1. Introduction

Advanced energy production/conversion technologies involve significantly high temperatures, mechanical loads and, in case of nuclear technologies, high irradiation doses. Moreover, potentially aggressive fluids (e.g. liquid metals, molten salts, and supercritical H₂O (SCW) or CO₂ are considered as cooling, heat-conversion and energy storage media, due to their beneficial and specific physicochemical properties [1-6].

Among these fluids, heavy liquid metals (HLM) such as Pb, Bi, Sn, Sb and their alloys are considered as promising functional media for advanced energy-related applications like fast neutron fission reactors (heat transport), spallation particles sources (neutron breeder), fusion reactors (tritium breeder,

neutron multiplier, heat transport), concentrated solar power (heat transport), methane cracking (reaction medium) and liquid metal batteries (electrode) [7-17].

The HLM-based technology was initially developed for fast reactor systems (i.e. Pb and Pb-Bi eutectic alloy). However, its implementation in commercial applications is mainly hindered by the long-term compatibility issues with the structural materials [18-33]. The high solubility of steel alloying elements, especially Ni and Cr, besides Fe itself, leads to corrosion attacks increasing with rising temperatures [28, 34-36]. One possible mitigation solution, valid within a limited temperature window, is an active fluid conditioning by means of an appropriate oxygen concentration in the HLM, allowing for an in-situ formation of protective oxide scales [29, 37, 38, 104]. Thus, below 500°C, both austenitic (e.g. 316) and ferritic-martensitic (F/M) steels (e.g. T91, HT9) are protected by Fe-based oxide scales, grown on the steel surface when exposed to oxygen-containing ($10^{-8} - 10^{-6}$ wt. %) molten Pb or Pb-Bi-eutectic (LBE) alloy. Studies, aimed at in-depth understanding of the steels-specific HLM-corrosion mechanisms, have been performed on austenitic steels at temperatures below 500°C in LBE, mainly with low and ultra-low oxygen concentrations ($\leq 10^{-7}$ wt.%) in order to accelerate the dissolution corrosion phenomenon [105-108]. These studies describe in detail the relationship between the steels microstructure and HLM corrosion. Moreover, they constitute the scientific support for the corrosion mitigation strategy, namely moderate operating temperatures (<450°C) and active control of the oxygen dissolved in LBE, which has been proposed in case of the accelerated-driven system technology demonstrator, the MYRRHA system (**M**ultipurpose **hY**brid **R**esearch **R**eactor for **H**igh-tech **A**pplications) [105, 106]. At temperatures exceeding 500°C, even a suitable oxygen concentration within the molten metal, does not yield protective oxide scale formation on austenitic steels. These suffer from severe dissolution attacks targeting mainly the nickel, which has the highest solubility of the alloying elements in HLM [19, 26, 27, 31, 33, 39, 109]. In contrast, the F/M steels between 500°C and 550°C develop thick Fe-based oxide scales, leading to the thinning of the metal part and negatively impacting the heat transfer [19, 27, 32], while at temperature $\geq 550^\circ\text{C}$ scale failure and dissolution attacks are likely to occur [19, 110]. Moreover, the creep resistance of the F/M steels dramatically drops because the protective layer breaks, above a critical stress threshold, resulting in a direct contact of the HLM with the unprotected steel surface [40, 41]. To provide protection at temperatures above 500°C a complementary corrosion mitigation solution is proposed, consisting in alloying the steels with strong oxide-forming elements, such as Si and Al [18, 42-45].

For almost two decades the F/M steels have been considered as candidates for in core components due to their better mechanical strength, heat load capability and irradiation resistance compared to austenitic stainless steels. Consequently, many research groups concentrated their efforts in developing and characterizing mainly Al- but also Si-containing F/M steels, including oxide-dispersion-strengthened (ODS) alloys. With appropriate Cr and Al or Si concentrations, these steels are protected by a continuous, thin and slowly growing oxide scale, when exposed to oxygen-containing molten Pb and LBE [46, 47]. As aluminium is especially beneficial in mitigating corrosion and excessive oxidation, researchers have focused their interest on Al-containing F/M steels [48-58]. An experimental criterion concerning the minimum Al concentration in Fe-Cr-Al-based ferritic alloys (C_{Al}), valid for the chromium content (C_{Cr}) in the range 10-25 wt.%, was defined for the temperature range 400°C to 600°C: $C_{\text{Al}} = 15.3 - 0.81 (C_{\text{Cr}}) + 0.0156 (C_{\text{Cr}})^2$ [wt.%] [59]. The effectiveness of Al addition was also proved up to 800°C, where Al-containing alloys, demonstrated excellent corrosion resistance [56-58].

However, the minimum Al and Cr concentration required to form protective slowly growing oxide scales can negatively impact the workability and mechanical properties (especially ductility) of the steels [60, 61]. In order to maintain the mechanical properties, the steels surface can be alloyed with aluminium only up to a depth of around 20-30 μm ; the Al concentration must be adequate, typically

5-8 wt. %, to form, through selective oxidation, a protective alumina scale during exposure to oxygen-containing HLMs. One approach was developed at Karlsruhe Institute of Technology (KIT): Al-containing layers (e.g. Al, Fe-Cr-Al-Y) are deposited by plasma spraying or electron beam assisted vapor deposition and subsequently modified by melting using intense pulsed electron beams. The approach, which is called “GESA method”, was successfully applied to both F/M and austenitic steels and Ni-based superalloys [62-66]. A continuous, slowly growing protective alumina scale was formed on T91 and 316 steels during exposure to oxygen-containing HLMs. A significant improvement in creep resistance in LBE, comparable with the creep resistance in air, was achieved by alloying the T91 steels surface with Al [41].

Despite the significant improvement of the corrosion and creep resistance of Al-alloyed F/M, either into the surface or into the bulk, the EU scientific community has abandoned the idea of using F/M steels as structural materials for the HLM cooled prototype nuclear systems, because of their high susceptibility to liquid metal embrittlement (LME) at temperatures below 400°C [67,68]. Nowadays, the designers of the HLM-cooled nuclear reactor prototypes are considering commercial austenitic steels (e.g. 15-15Ti and 316) as structural materials. However, all these materials considered also for critical components of commercial nuclear reactor systems, require a dramatic improvement of their corrosion and mechanical properties.

Potential candidates for structural materials in energy-related applications based on HLM technology, including nuclear reactors, are alumina-forming austenitic (AFA) steels. These steels, developed initially at Oak Ridge National Laboratory (ORNL) for applications in aggressive environments in energy production (e.g. fossil-fired power generation systems) and in chemical processing plants, were designed as “oxidation- and creep-resistant” alloys [69-71]. Having the prerequisite of the preservation of an austenite single-phase matrix, which can be fulfilled by an appropriate ratio of austenite- and ferrite- stabilizer elements, the balance between oxidation resistance and mechanical properties was obtained in a broad compositional range of Fe-(12-35)Ni-(12-19)Cr-(2.5-4)Al-(0.6-3)Nb-Mn-Mo-W-Si,B,C,Ti,Zr [72]. The impact of the second-phases, such as carbides (e.g. Cr_{23}C_6 , NbC), Laves phase and γ' phase, on the mechanical properties, especially at high temperatures and such as B2-NiAl phase on alumina formation and stability, was intensively studied [69-78]. The influence of minor elements additions, such as Y, La, Hf, B, C, Ti, Cu, Mn, Mo, Si, on corrosion and mechanical properties at high temperatures and on workability was also investigated [79-87].

Based on the Ni content and the targeted alumina formation temperature range, the AFA steels are classified into three categories: (i) high Ni-content (30-35 wt.%), with relatively high strength, for applications in the temperature range ~ 750 -850°C, (ii) standard Ni-content (20-25 wt.%) for applications in the temperature range ~ 750 -950°C and (iii) low Ni-content (12-15 wt.%), for the temperature range ~ 650 -700°C [72].

The corrosion tests of the AFA steel grades, performed in air and air + water vapor, have shown their excellent corrosion behaviour especially at higher temperatures ($>800^\circ\text{C}$), due to the formation of an alumina scale [69, 78, 79, 82, 88]. However, tests performed at lower temperatures (550°C) in air, revealed the formation of only Fe-based oxide without traces of alumina [89].

In searching for AFA potential application in industrial sectors, in which corrosive environments are involved, promising results were obtained during corrosion tests performed in SCW conditions [90], sulfidation–oxidation conditions [91], supercritical CO_2 conditions [92], molten sodium sulphate [93] and metal dusting conditions [94].

AFA steels were also exposed to molten lead with 10^{-7} wt.% oxygen at 550°C for up to one year. It was found that a thin Al_2O_3 layer protected the AFA steel with lower Ni content (14 wt.%) while AFA steel containing 20 wt.% Ni displayed localized dissolution attacks [95]. However, the former alloy (Fe-

14.4Cr-13.9Ni-2.49Al-MnMoNbSi), while revealing excellent corrosion resistance, showed a phase transformation from austenite to ferrite in around 17% of the volume. Other results published in 2016 led to the conclusion that Fe-14Cr-25Ni-3.5Al-MnMoNb showed promising corrosion behaviour, while exhibiting few dissolution zones, during exposure to oxygen-containing molten Pb-Bi eutectic at 520°C [39].

In the view of this present state the focus of the Karlsruhe Institute of Technology research for HLM applications has been directed to a systematic program of developing AFA steels compatible with such environments. The first aim of the program is to determine the concentration ranges of the alloying elements (Cr, Al and Ni), for which quaternary Fe-Cr-Al-Ni-based model alloys exhibit corrosion resistance in molten Pb, while preserving the austenitic structure as the alloy matrix. This article presents the results regarding the corrosion tests performed in oxygen-containing molten Pb on model alloys (Fe-Cr-Al-Ni), which are designed considering the above mentioned requirements. From the results obtained appropriate concentration ranges of the alloying elements have been selected and are proposed as the backbone for the development of AFA steels with corrosion resistance in HLMs environment.

2. Materials design and experimental procedure

2.1 Alloys design

The exploration and the development of AFA steels have been focused so far mainly on the replacement of Ni-base alloys or austenitic steels in different environments [69, 78, 79, 82, 88-94]. However, the direct transfer of AFA steels engineering-knowhow, related to these environments, to applications in HLMs is questionable, because of the additional physical and chemical interactions implied by the contact with such media. Therefore, the development of dedicated AFA steels, which are able to withstand the dissolution attack of the HLMs while keeping the austenitic phase, is required.

Since corrosion resistance is a basic requirement for materials in contact with HLMs, the design activity is directed towards finding an appropriate set of composition ranges for the quaternary Fe-Cr-Al-Ni, where Ni acts as austenite stabilizer, Al as ferrite stabilizer and alumina layer former, and Cr as ferrite stabilizer, chromia layer former and provider of third-element effect (TEE). Initially, TEE was observed in Fe-Al alloys, where the addition of Cr significantly decreased the critical Al-content needed to form protective Al_2O_3 layer [98, 111]. The effect, frequently discussed in literature and observed also in other alloy systems, including alumina-forming austenitic steels [71], was associated with: transition from internal to external oxidation, inhibition of the Fe external oxidation and nucleation of α - Al_2O_3 inside of the corundum-type structure of Cr_2O_3 [99, 112, 113]. TEE is important from the alloy-design viewpoint due to the fact that Al is three times more effective in stabilizing the ferrite phase [97], which means that, for the same Ni content, the addition of 1 wt.% Al would require a corresponding decrease of 3 wt.% of Cr in order to avoid ferrite phase formation.

For the current study, two requirements are taken into consideration: (i) to form stable passivating oxide scales during exposure to oxygen containing molten Pb at temperatures above 550°C and (ii) to preserve the austenitic phase as the alloy matrix microstructure.

Four Cr concentrations, namely 12, 14, 15 and 16 wt. %, are selected to ensure a strong third element effect on the alumina formation and, at the same time, to limit the formation of ferrite and Cr-rich phases. An Al concentration range between 2 and 4 wt.% is chosen to sustain the formation of protective alumina scale and to avoid the excessive ferrite formation and the alloy embrittlement. The

Ni composition varies between 20 and 29 wt.% to stabilize the austenite structure as the alloy matrix, during exposure to the oxygen-containing molten Pb at 550-600°C.

Based on the entries above, the phase-stability diagrams at 550°C and 600°C for the Fe-12Cr-xAl-yNi, Fe-14Cr-xAl-yNi, Fe-15Cr-xAl-yNi and Fe-16Cr-xAl-yNi systems are calculated using the commercial software Thermo-Calc. As an example, the superimposed calculated phase diagrams for Fe-(12,14,15,16)Cr-xAl-yNi systems at 600°C are shown in Fig.1. Twelve alloy compositions, with the general formula Fe-(12-16)Cr-(2-4)Al-(20-29)Ni, are taken lying close to the separation lines between the stability domains of the austenite (γ) and austenite plus ferrite ($\gamma+\alpha$), for studying their corrosion resistance and microstructure stability, during exposure to oxygen-containing molten Pb at 550°C and 600°C (Fig.1).

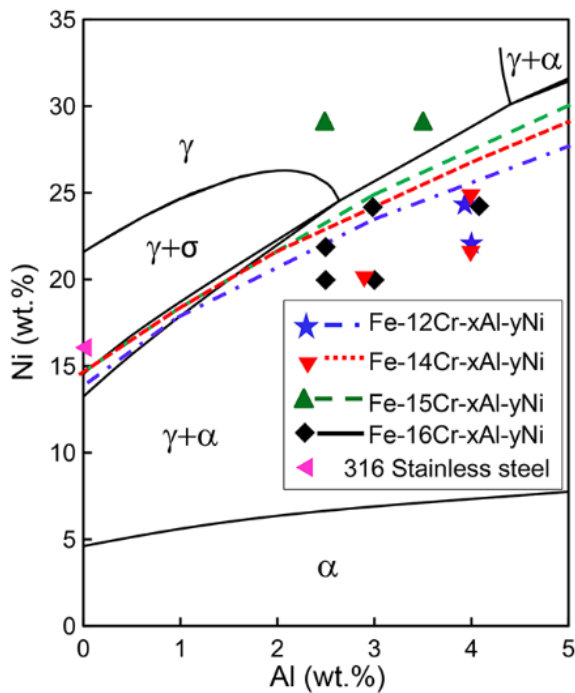


Fig. 1. Calculated phase diagrams for the model Fe-(12,14,15,16)Cr-xAl-yNi systems at 600°C, with the coordinates of the selected nominal compositions for this study and the 316 steel indicated: ★ – H48, H51; ▼ – H45, H49, H52; ▲ – H55, H56; ◆ – H46, H47, H50, H53, H54; ◀ – 316 (γ - austenite, α - ferrite, σ - Cr-rich phase)

Stainless steel industry developed methods based on empirical maps for the estimation of the type of phases and their amount, as a function of the chemical composition of the steels. The most popular empirical map is the Schaeffler diagram. With this diagram a rough evaluation of the phase constitution of the stainless steels at ambient temperature, following the water cooling from liquid phase or from austenite domain ($>1200^\circ\text{C}$) can be made using nickel and chromium equivalents [96, 97]. Fig. 2 depicts the Schaeffler diagram where the twelve model alloys selected for the current corrosion study are indicated. According to this diagram, all model alloys selected have an austenite structure at room temperature. For comparison, two commercial stainless steels (310 and 316) are also marked in the diagram.

Both design tools are of value for the current study since the Schaeffler diagram can estimate the initial (before tests) phase constitution, while Thermo-Calc calculations can predict the phase equilibrium after the long-term exposure at 550°C and 600°C.

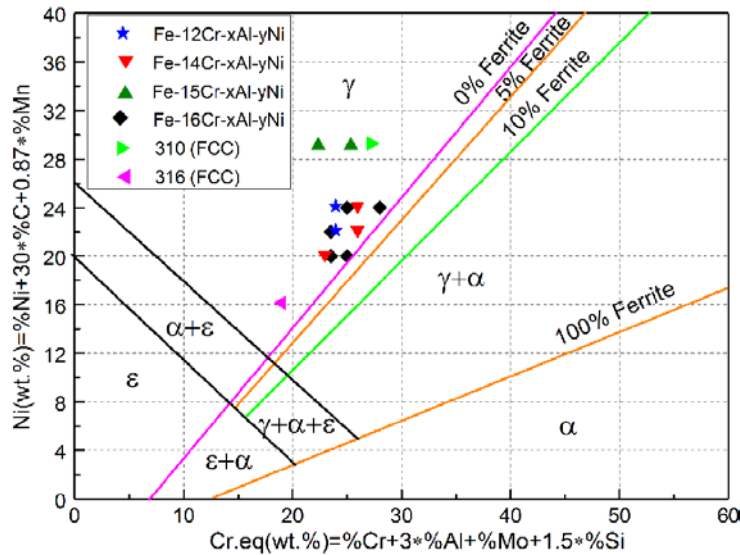


Fig. 2. Schaeffler constitution diagram including the coordinates of the model Fe-Cr-Al-Ni alloys and of two references: stainless steels 310 and 316 (γ - austenite, α - ferrite, ε - martensite).

2.2 Alloys synthesis

The model alloys are prepared as ingots by arc-melting using a non-consumable tungsten electrode in an argon atmosphere using high purity elements. The prepared alloy ingots have been flipped over and remelted eight times in a water-chilled copper mold, to facilitate alloy homogenization. The as-solidified ingots have been sealed in quartz tubes, under argon atmosphere and further annealed for homogenization at 1250°C for 2 hours, followed by water quenching.

The nominal and measured compositions of the alloys, determined by energy dispersive X-ray spectroscopy (EDS), are shown in Table 1. The Cr, Al and Ni contents are measured within 1 wt.% accuracy.

Table 1 Chemical composition of Fe-Cr-Al-Ni model alloys measured with EDS (wt.%)

Code	Nominal composition	Al (wt.%)	Cr (wt.%)	Ni (wt.%)	Fe
H45	Fe-14Cr-3Al-20Ni	2.8	14.4	19.5	Balance
H46	Fe-16Cr-2.5Al-20Ni	2.3	16.6	19.6	Balance
H47	Fe-16Cr-3Al-20Ni	2.7	16.6	21.7	Balance
H48	Fe-12Cr-4Al-22Ni	4.0	12.2	21.3	Balance
H49	Fe-14Cr-4Al-22Ni	4.2	14.4	21.2	Balance
H50	Fe-16Cr-2.5Al-22Ni	2.5	16.5	21.4	Balance
H51	Fe-12Cr-4Al-24Ni	4.3	12.3	23.3	Balance
H52	Fe-4Al-14Cr-24Ni	4.3	14.3	23.4	Balance
H53	Fe-16Cr-3Al-24Ni	3.2	16.5	23.3	Balance
H54	Fe-16Cr-4Al-24Ni	4.3	16.3	23.4	Balance
H55	Fe-15Cr-2.5Al-29Ni	2.5	15.4	28.3	Balance
H56	Fe-15Cr-3.5Al-29Ni	3.8	15.2	28.5	Balance

2.3 Corrosion tests

The experiments have been performed in stagnant molten Pb with 10^{-6} wt.% oxygen in the COSTA facility, at 550°C and 600°C for 1000 hours [29].

Alumina crucibles were first filled with 200 g Pb, then placed on a Ni-tray in a quartz-tube inserted into a tube furnace. The oxygen content in the liquid Pb was controlled via the Ar/Ar+H₂ content in the gas phase. The oxygen activity of the gas phase was measured at the outlet of the quartz-tube with an oxygen sensor and displayed as oxygen partial pressure. The liquid Pb was exposed to reducing conditions at 600°C for 3 days, followed by 7 days at exposure conditions (regarding temperature and oxygen content).

The prepared alloy ingots were cut into discs of around 10 mm diameter and 1.2 mm thickness. A hole with diameter of 1.5 mm was drilled on each specimen near the edge. All specimens were grounded to a 1200 grit surface finish. Just before testing, the specimens were successively cleaned with water, acetone and ethanol in an ultrasonic bath, and dried. Each specimen was hanged using the hole and fastened to the alumina holders with Mo-wire to prevent floating.

In order to introduce the specimens into the pre-conditioned liquid Pb, a dedicated glove-box was used as air lock, conditioned to a similar oxygen partial pressure as in the quartz-tube. After connecting the glove-box to the quartz-tube, the Ni-tray with all molten Pb-containing crucibles was transferred into the glove box. All the specimens were placed in the crucibles and fully immersed in the molten Pb. During this loading phase, which took about 3 minutes, the temperature of the liquid Pb dropped to about 450-500°C. After putting back the Ni-tray with all crucibles and specimens into the quartz-tube, the temperature recovered to the set value within ~ 10 min, while the oxygen partial pressure at the quartz-tube outlet recovered within less than 2 hours. During exposure tests, the oxygen partial pressure was continuously measured and kept constant at the set value.

The extraction of the specimens from the crucibles was performed using the same glove-box, conditioned in the same way as for the loading process. None of the specimens was found floating and the surface of the molten lead in all crucibles was shining metallic silver-gray and free of oxides.

2.4 Samples characterization

The evaluation of the specimens, before and after exposure, has been performed using scanning electron microscopy (SEM), equipped with an energy dispersive X-ray spectroscopy (EDS) system, and X-ray diffractometry (XRD) with θ - 2θ conventional geometry, 0.02° step size, 6 s per step, 10 - 90° 2θ range and Cu-K α radiation ($\lambda = 1.5406 \text{ \AA}$).

All samples were visually examined after the extraction from the molten lead. The aspect of the samples, depends on the interaction between the molten Pb and the alloy surface, i.e. the degree of wettability. In accordance with their visual aspect, the exposed samples have been classified in two categories: (i) samples with almost Pb-free surface or with only few, small areas covered by a thin solid Pb-layer, and (ii) samples with large regions of the surface covered by an adherent and thick Pb-layer. For the first category, it can be assumed that, under the experimental conditions, there is no chemical reaction between the sample and the molten lead. Such non-wetting behaviour is due to the formation of a continuous and protective oxide layer on the sample surface [114]. For the second category, one can suppose a reactive wetting behaviour, due to a reaction at the solid-liquid interface, such as the simple dissolution of the sample alloying elements into the liquid, accompanied by changes of the surface roughness and the contact angle [115].

However, the morphology of the entire surface of the specimens needs to be evaluated in detail by SEM since the aim of this study is to select the model Fe-Cr-Al-Ni alloys exhibiting corrosion resistance in molten Pb. Moreover, the chemical and phase compositions of the oxide scale, grown on these

samples, need to be analysed with EDS and XRD characterization methods. Such analyses demand surfaces, which are free from residual adherent Pb in order to make the oxide scale itself accessible for inspection. Therefore, all samples were cleaned from the remaining adherent lead by immersing them for 15 min into a solution of ethanol, acetic acid and hydrogen peroxide (1:1:1). The cleaning solution does not react with the oxide scale or the alloy elements. This cleaning method is adopted as a standard procedure [116] and is used by many research groups [50, 56, 59, 117].

Following the surface evaluation using XRD and SEM/EDS, the specimens were electroplated with ~ 40 μm nickel layer, cross-sectioned by standard metallographic techniques and further analysed by SEM/EDS.

3. Results

3.1 Alloy microstructure characterization before exposure

Before exposure, the microstructure of all samples consists of large grains (0.3-2 mm), as illustrated in Fig.3 by some examples. Few randomly distributed oxide inclusions (Al-rich) with the size $\leq 1 \mu\text{m}$ have been observed. Taking into consideration the large dimension of the grains and the very low density of the structural and chemical defects, the general corrosion behaviour of the alloys will be mainly influenced by alloys chemical composition and structure.

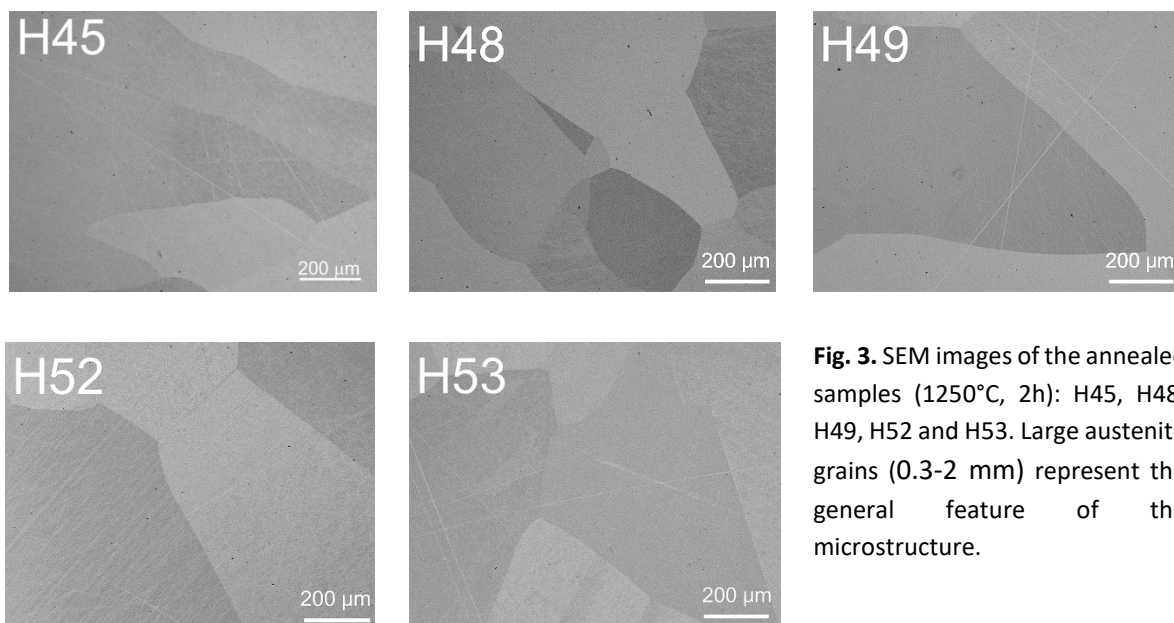


Fig. 3. SEM images of the annealed samples (1250°C, 2h): H45, H48, H49, H52 and H53. Large austenite grains (0.3-2 mm) represent the general feature of the microstructure.

XRD evaluation confirms the prediction of Schaeffler diagram exhibiting for all samples a single-phase austenite structure ($\gamma\text{-Fe}$, face centered cubic – f.c.c) without any secondary metallic phases (Fig. 4).

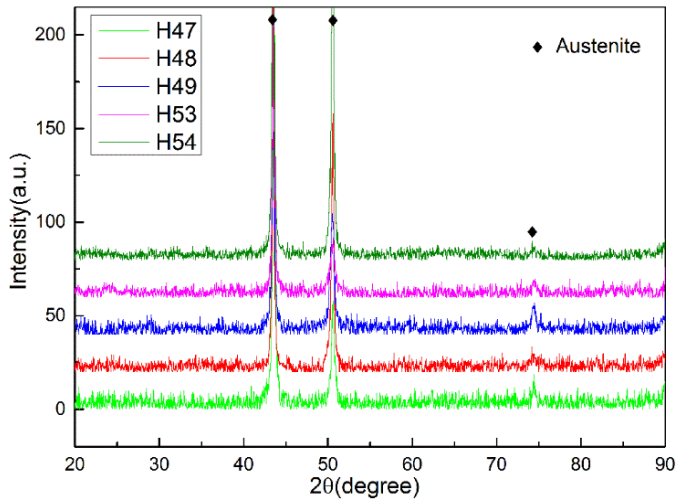


Fig. 4. Examples of XRD patterns of the annealed samples H47, H48, H49, H53 and H54 displaying austenite single phase.

3.2 Corrosion experiments at 550°C

The preliminary conclusions of the visual inspection (adherence of Pb), performed immediately after the specimens extraction from the molten lead, were confirmed with good accuracy by the SEM surface analysis of the specimens cleaned from remaining adherent Pb. The samples with almost Pb-free surface form protective oxide scale, while the samples with large surface regions covered by thick Pb-layer suffer dissolution attacks.

Dissolution attacks were observed on the samples with 12 wt.% Cr (H48 and H51) and on two others containing 14 wt.% Cr (H49 and H52). While in the case of the H48 and H51 alloys the dissolution attacks are widespread (~ 90% of the surface) and the dissolution layer thickness reached up to 100 μm (H48), the specimens made of the H49 and H52 model alloys display localized attacks with depths up to 10 μm , on ~ 30-40% of their total surface (Fig. 5). The corrosion layers are depleted mainly in Ni, leading to their ferritization and concomitant lead penetration. Model alloys with 14 wt.% Cr reveal a thin oxide layer (<100 nm), not covering the alloy surface uniformly but featuring spots with dissolution attack.

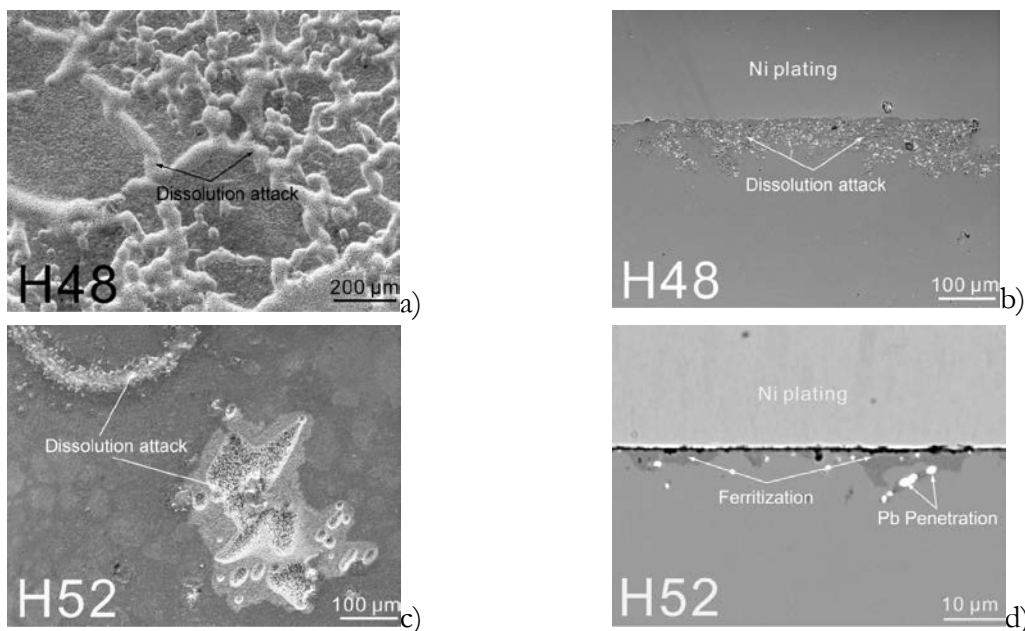


Fig. 5. Dissolution attacks observed on the surface and on the cross section of H48 (a, b) and H52 (c, d) specimens exposed to molten Pb with 10^{-6} wt. % oxygen at 550°C for 1000h.

Eight samples have developed continuous and protective thin oxide scales during exposure to molten lead with 10^{-6} wt.% oxygen at 550°C, for 1000h (Fig. 6). These samples are made of the following alloys: H45 (Fe-14Cr-3Al-20Ni), H46 (Fe-16Cr-2.5Al-20Ni), H47 (Fe-16Cr-3Al-20Ni), H50 (Fe-16Cr-2.5Al-22Ni), H53 (Fe-16Cr-3Al-24Ni), H54 (Fe-16Cr-4Al-24Ni), H55 (Fe-15Cr-2.5Al-29Ni) and H56 (Fe-15Cr-3.5Al-29Ni). Few Fe-rich oxide protrusions (magnetite) have been identified on the surface of H45, H46, H53 and H56 samples. They may come from structural and chemical inhomogeneity, such as grain boundaries.

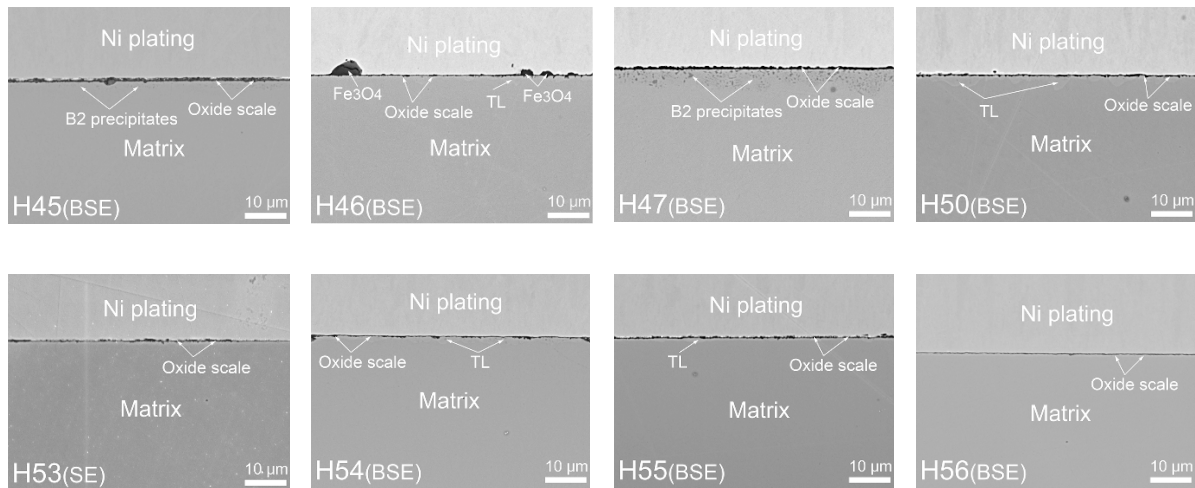


Fig. 6. SEM cross section images of the samples displaying continuous and protective oxide scale after exposure to molten Pb with 10^{-6} wt. % oxygen at 550°C for 1000h (H45, H46, H47, H50, H53, H54, H55, H56); TL: transitional layer (SE: secondary electrons image; BSE: back-scattered electrons image).

A common characteristic of all these samples is a quasi-continuous transitional layer with bright aspect, beneath the oxide scale, consisting of a Fe- and Ni-enriched matrix (due to Cr- and Al- diffusion to the surface), in which B2-(Ni,Fe)Al precipitates with darker aspect are randomly distributed. In some spots of the transitional layer, at the interface with the oxide scale, slightly oxidized Cr-enriched precipitates are observed as for the H47, H50 and H54 alloys. The thickness of the transitional layer, which can be considered as the interface between the oxide scale and the bulk alloy, varies between ~1-2 μm .

EDX elemental mapping and line scans, performed on the cross sections, revealed that the thin and protective oxide scales (<100 nm), which have grown during the exposure to oxygen-containing molten Pb, are based on Al- and Cr-oxides, which is illustrated in Fig. 7 and Fig. 8. The oxygen signal maximum in the EDX line scans (Fig. 8) indicating the oxide scale, is overlapping both Cr and Al maximums. Moreover, the maximums of the signals corresponding to aluminium and chromium either overlap (e.g. H46) or are slightly shifted, with Cr peak appearing first (e.g. H50).

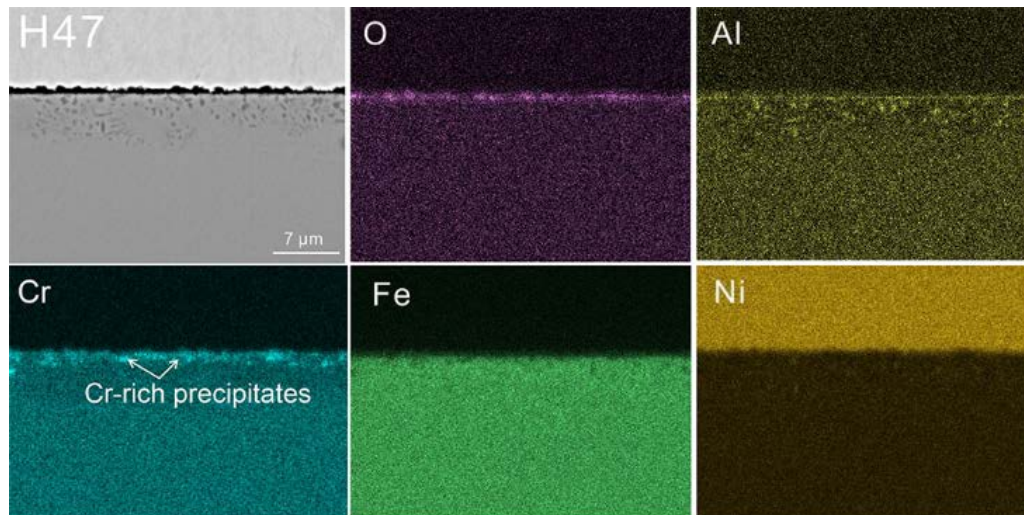


Fig. 7. Elemental map of H47 exposed to molten Pb with 10^{-6} wt.% oxygen at 550°C for 1000h. The sample is protected by Al-Cr-base oxide scale; underneath the scale B2-(Ni,Fe)Al precipitates are observed in the Ni-enriched transitional layer. Moreover, slightly oxidized of Cr-rich precipitate are visible just below the scale.

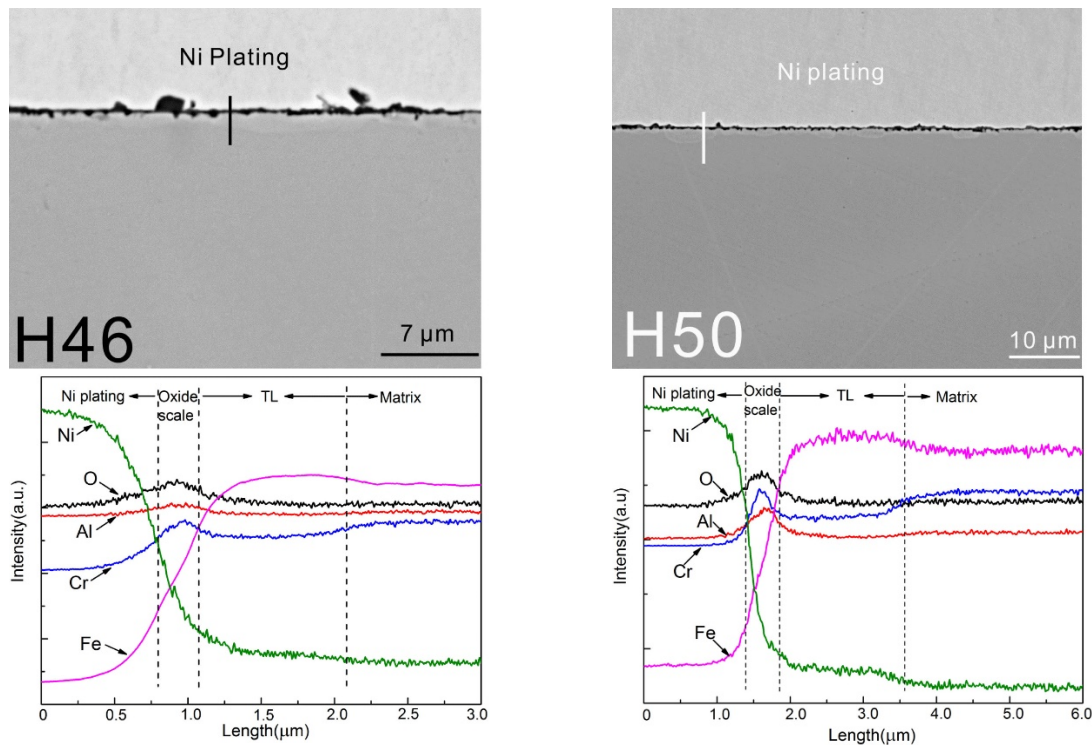


Fig. 8. SEM cross section images and corresponding EDX line scans of oxide scales grown on H46 and H50 samples exposed to molten Pb with 10^{-6} wt.% oxygen at 550°C for 1000h. The samples are protected by an Al- and Cr-rich oxide scale. The transitional layer (TL) enriched in Ni and Fe, underneath the scale is also visible.

The XRD patterns provide information about the phase composition of the oxide scales and of the substrate (Fig. 9). While the Cr- and Al-maximums are clearly visible at the scale region in all EDX line scans, the X-ray diffraction signals coming from the scales are weak as a consequence of the very small thicknesses and possible structural disorder of the scales. However, based on the current results, two corundum-type crystalline structures (rhombohedral lattice system) are identified as the main constituent phases of the oxide scales, one being Cr_2O_3 and the other $\text{Al}_2\text{O}_3\text{-Cr}_2\text{O}_3$ solid solution. The 100% intensity peak of Cr_2O_3 , corresponding to (104) lattice plane, is located at $2\theta = 33.61^\circ \pm 0.02^\circ$, while the 100% intensity peak of the $\text{Al}_2\text{O}_3\text{-Cr}_2\text{O}_3$ solid solution, corresponding to the same lattice

plane, is located in the range between $34,44^\circ$ and $34,65^\circ$. Peaks corresponding to the magnetite (Fe_3O_4) are also present in the XRD patterns of the samples displaying spots with Fe-rich oxide protrusions on their surface.

The transitional metallic layer, observed underneath the oxide scale, consists of an austenite matrix (PDF no. 33-397) with B2-(Ni,Fe)Al precipitates (PDF no. 47-1126). Neither peaks of ferrite, nor Cr-rich σ -phase were observed.

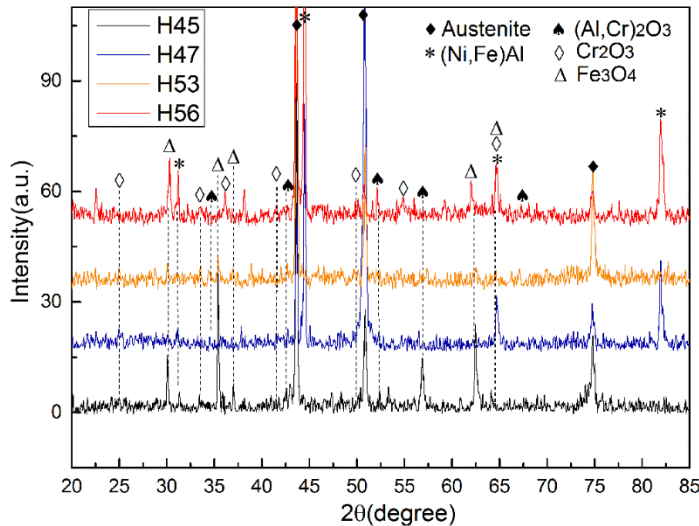


Fig. 9. Examples of XRD patterns obtained from the samples exposed to molten Pb with 10^{-6} wt. % oxygen at 550°C for 1000h.

3.3 Corrosion experiments at 600°C

The samples with Cr content of 12 wt.% (H48, H51) and 14 wt.% (H45, H49, H52), together with one sample containing 16 wt% (H47) have failed to develop protective scales, showing extensive dissolution attacks instead.

The other six specimens, made from Fe-Cr-Al-Ni-based model alloys, have been passivated during their exposure to molten lead with 10^{-6} wt.% oxygen at 600°C for 1000h, by in-situ grown oxide scales. The nominal chemical compositions of the “surviving” specimens are the following: Fe-16Cr-2.5Al-20Ni (H46), Fe-16Cr-2.5Al-22Ni (H50), Fe-16Cr-3Al-24Ni (H53), Fe-16Cr-4Al-24Ni (H54), Fe-15Cr-2.5Al-29Ni (H55), Fe-15Cr-3.5Al-29Ni (H56). SEM cross sectional images of these samples are shown in Fig. 10.

As in the case of the specimens exposed to molten Pb at 550°C , the preliminary conclusions, after the visual inspection of the samples exposed at 600°C , were confirmed by SEM surface analysis of the specimens cleaned from remaining adherent Pb.

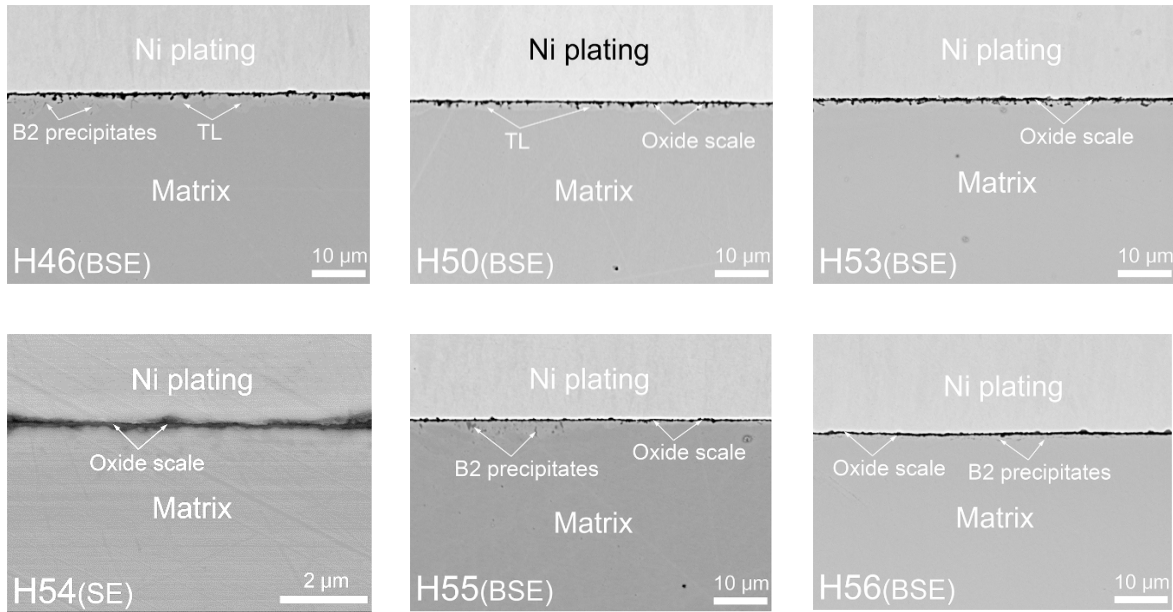


Fig. 10. SEM cross section images of the passivated specimens, during their exposure to molten lead with 10^{-6} wt.% oxygen at 600°C for 1000h (H46, H50, H53, H54, H55, H56); TL: transitional layer (SE: secondary electrons image; BSE: back-scattered electrons image).

The protective oxide scales, based on Al- and Cr- oxides, have thicknesses in the range of ~ 50-100 nm (Fig. 11, 12). As can be observed in the line scans depicted in Fig. 11, the signal corresponding to chromium reaches a maximum before that corresponding to aluminium and both are overlapped by the maximum of the oxygen signal. A transitional metallic layer, enriched in Fe and Ni, with B2-(Ni,Fe)Al precipitates and, in some spots, with slightly oxidized Cr-rich precipitates, is present below the protective scale (similarly to the case of samples exposed at 550°C). The thickness of the transitional layer is not uniform and varies from tens of nanometers to two microns.

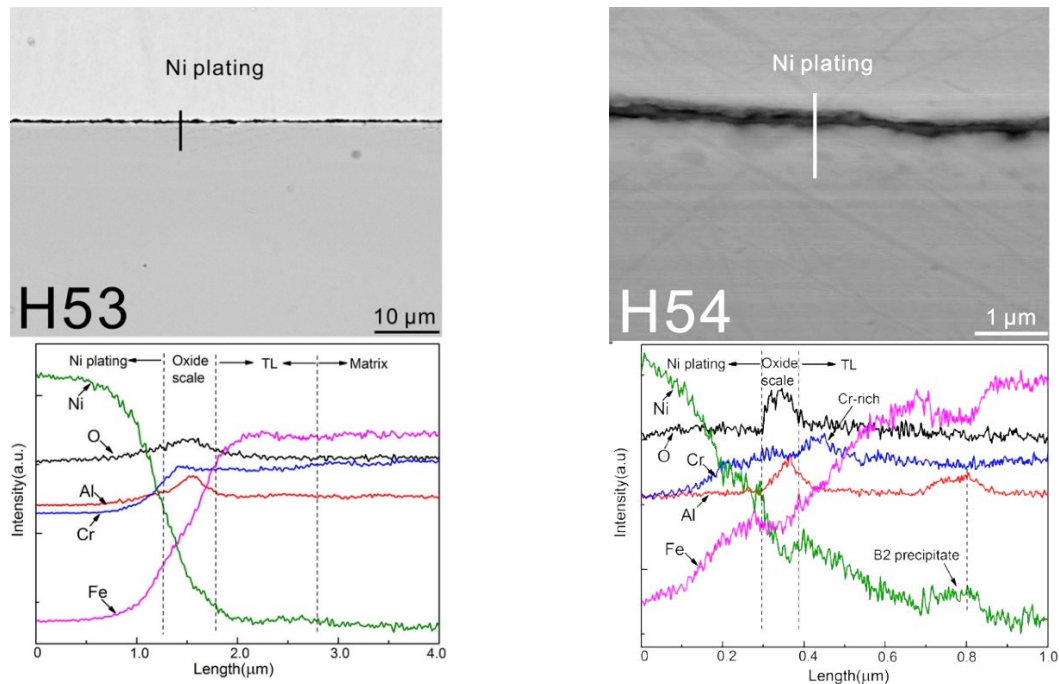


Fig. 11. SEM cross section images and corresponding EDX line scans of oxide scales grown on H53 and H54 samples exposed to molten Pb with 10^{-6} wt.% oxygen at 600°C for 1000h. The samples are protected by an Al- and Cr-base oxide scale. Underneath also a transitional layer (TL) enriched in Ni and Fe is visible, containing B2-(Ni,Fe)Al precipitates. In case of H54, Cr-enrichment can be observed just below the scale.

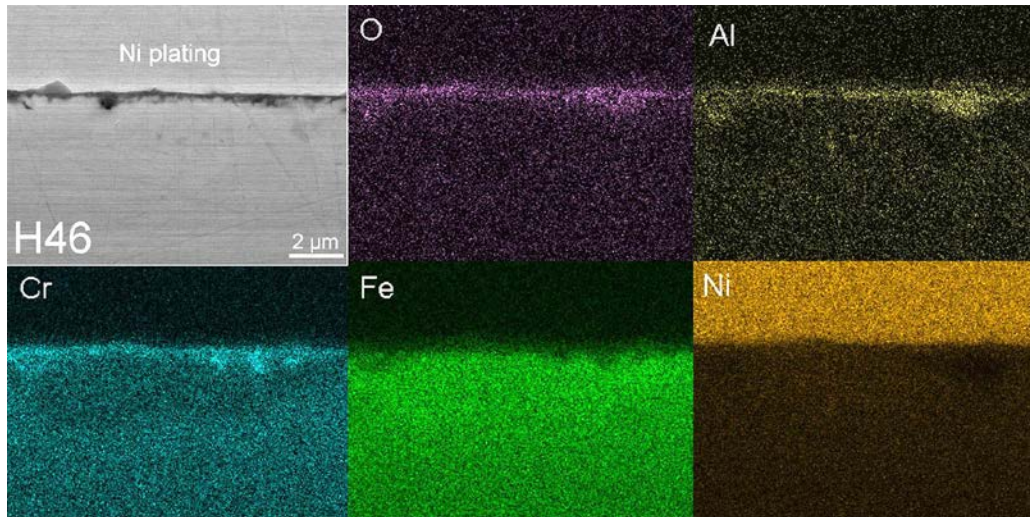


Fig. 12. Elemental map of H46 exposed to molten Pb with 10^{-6} wt.% oxygen at 600°C for 1000h. The protective scale is an Al-Cr-base oxide; underneath the scale, B2-(Ni,Fe)Al precipitates are observed in the transitional layer.

According to XRD analysis, the oxide scale is made of Cr_2O_3 and $\text{Al}_2\text{O}_3\text{-Cr}_2\text{O}_3$ solid solution, displaying the (104) diffraction peak at $2\theta = 33,61^\circ \pm 0.02^\circ$, in case of Cr_2O_3 , and between $34,50^\circ$ and $34,73^\circ$ in case of the $\text{Al}_2\text{O}_3\text{-Cr}_2\text{O}_3$ solid solution. The peaks corresponding to austenite and B2-(Ni,Fe)Al phase arise from the transitional layer and the bulk matrix (Fig. 13).

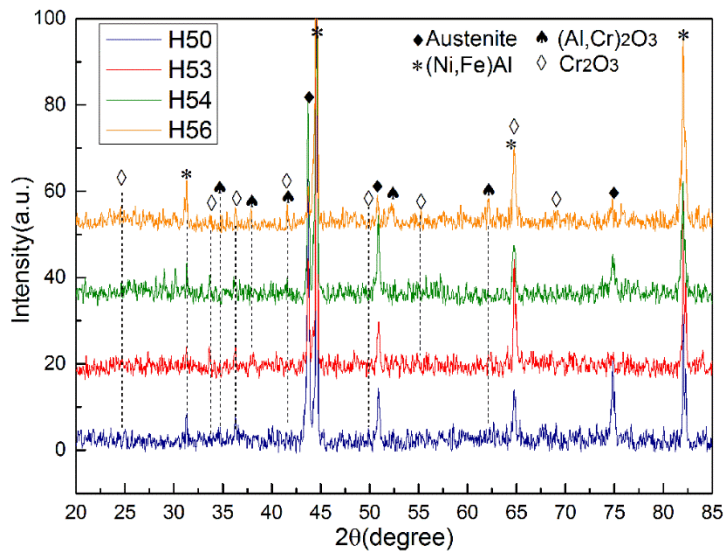


Fig. 13. Examples of the XRD patterns obtained from the samples exposed to molten Pb with 10^{-6} wt. % oxygen at 600°C for 1000h.

After removal by grinding of the oxide scale and of $\sim 20 \mu\text{m}$ metal layer, the structure of the bulk samples exposed to oxygen containing molten lead for 1000h at 600°C is analysed by X-ray diffraction. The austenite structure is preserved as a matrix and a secondary phase precipitates in all samples. The peaks corresponding to the precipitates can be assigned to the intermetallic compound $\text{Ni}_3(\text{Al,Fe})$ owing f.c.c. crystalline structure.

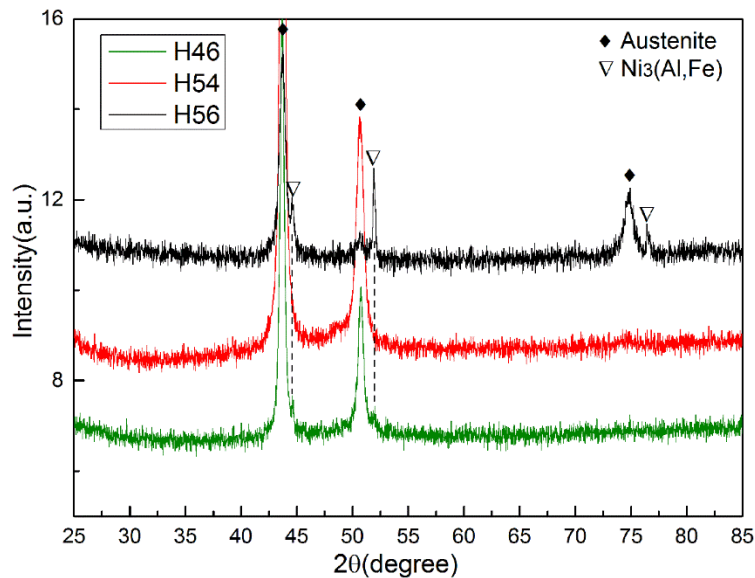


Fig. 14. XRD patterns of the H46, H54 and H56 alloys exposed at 600°C for 1000h to molten Pb with 10^{-6} wt.% oxygen. The oxide scale and $\sim 20\ \mu\text{m}$ metal layer were removed by grinding before the XRD analysis. The microstructure of the exposed alloys consists in the austenite (γ) and γ' -Ni₃(Al,Fe) phases.

4. Discussion

The goal of the study is to determine the critical concentrations of Al, Cr and Ni, at which the quaternary Fe-Cr-Al-Ni model alloys are able to form stable protective oxide scale while preserving an austenite matrix during the exposure to molten Pb containing 10^{-6} wt.% oxygen at 550 and 600°C.

From the twelve alloys selected for this study, six alloys, namely Fe-16Cr-2.5Al-20Ni (H46), Fe-16Cr-2.5Al-22Ni (H50), Fe-16Cr-3Al-24Ni (H53), Fe-16Cr-4Al-24Ni (H54), Fe-15Cr-2.5Al-29Ni (H55), Fe-15Cr-3.5Al-29Ni (H56), have shown corrosion resistance during the exposure to molten Pb containing 10^{-6} wt.% oxygen for 1000 hours at 550 and 600°C, by forming protective oxide scales based on chromia and alumina.

In case of the alloys designed to form passivating alumina scales, Cr is added in order to reduce the critical concentration of Al necessary to form such scales (so called third-element effect) [98, 99, 112, 113]. However, both Al and Cr are elements which stabilize the ferrite phase relative to austenite phase in steels. Moreover, the effect of Al is approximately 2-3 times stronger than the Cr effect [73, 97], which means that the Al addition should be accompanied by a corresponding Cr decrease, in order to avoid ferrite formation. In conclusion, both elements are needed to achieve alumina scale formation, but a balance between their summed concentrations relative to Ni concentration needs to be carefully considered in order to maintain the austenite phase as the alloy matrix.

For maintaining a single-phase austenitic matrix, the substitution of Fe with Ni between 20 and 29 wt.% has been designed for counterbalancing the total amount of Al and Cr. Ni addition moreover offers a beneficial effect on the oxidation behaviour of Fe-Cr-Al-Ni-based alloys since, Ni, together with Al, forms a B2-NiAl compound, which acts as an Al reservoir for alumina scale formation and growth. A recent study performed on “composition spread alloy films” oxidized at 427 °C in dry air showed that the addition of Ni above a certain threshold value abruptly decreases the Al critical concentration necessary to form the alumina scale [100]. A possible explanation could be the fact that a higher Ni content may decrease the oxygen solubility/diffusivity in the alloy, favoring external alumina formation, and may increase the Cr activity [101].

Generally, minimum values of Cr and Al concentrations are required to promote the growth of a passivating oxide scale on Fe/Ni-based alloys during exposure to oxygen containing environments. As determined during the presented experimental work, the Al concentration for the formation of passivating oxide scale at both exposure temperatures (550°C and 600°C) varies in the range of 2.3 - 4.3 wt. %, while the Cr concentration is in the range of 15.2 - 16.6 wt.%. Chromium concentrations of ~ 12 wt.% (at 550 and 600°C) and of ~ 14 wt.% (at 600°C) are demonstrated in the experiments to be insufficient to sustain the formation of a protective alumina scale. The Ni depletion with the

subsequent ferritization of the dissolution layer and the concomitant penetration of lead into the bulk material are the major corrosion phenomena, which characterize the corrosion behaviour of the model alloys containing 12 wt.% and 14 wt.% Cr.

Corroborating the data from the EDX line scans, EDX elemental mappings and XRD patterns it can be concluded that the protective oxide scale, grown on six alloys (with Cr concentration in the range of 15.2-16.6 wt.%) after 1000h exposure to oxygen-containing molten lead at 550°C and 600°C, is based on Cr_2O_3 and Al_2O_3 . It is presumed that a continuous and protective Cr_2O_3 layer is formed at first, before the Al_2O_3 layer establishes, which is due to the higher content of Cr atoms relative to Al atoms in the austenite matrix and the higher growth rate of Cr_2O_3 relative to Al_2O_3 . At the bottom and underneath the chromia layer, the oxygen partial pressure drops to a level that favours the selective oxidation of Al and the predominantly inward growth of the Al-base oxide. Hence, Cr_2O_3 serves as a first protective layer and as oxidation retardant and, having a corundum-type structure, as nucleation centres for the α - Al_2O_3 formation. The small thickness of the protective oxide scale (<100 nm) and the presence of the Al_2O_3 - Cr_2O_3 solid solution indicate a slow oxidation kinetics. The reasons for this phenomenon may reside in the low oxygen solubility/diffusivity and sluggish aluminium diffusion in the austenite phase [102]. Moreover, a linear relationship between the diffraction angle of the (104) peak and the Cr_2O_3 content in the solid solution was recently reported [103]. The average amount of Cr_2O_3 in the Al_2O_3 - Cr_2O_3 solid solution found in the scales of the Fe-Cr-Al-Ni model alloys, estimated by using this relationship is ≈ 40 wt.% at 550°C and ≈ 35 wt.% at 600°C.

The transitional metallic layer beneath the oxide scale is enriched in Ni and Fe, owing to the diffusion of Cr and Al towards the oxide scale with the subsequent decrease of their content in the transitional layer (Fig. 8, Fig. 11a). Likewise, Ni and Fe enrichment are underlining the efficiency of the formed oxide scale as a diffusion barrier for these two elements. However, a decrease of the Al concentration in the region underneath the oxide scale to values below its solubility limit in austenite, may limit (hinder) the healing process in case of the accidental scale loss. The presence of the B2-(Ni,Fe)Al precipitates in the transitional layer (Figs. 7, 11b and 12) is not yet understood. It is presumed that, due to the faster diffusion of Cr atoms towards the surface during the transient stage of the oxidation, the concentration of Al may locally exceed the solubility limit in austenite (~ 2.5 wt.%) leading to the precipitation of the intermetallic B2-(Ni,Fe)Al phase. These precipitates are considered to act as an Al reservoir during the formation and growth of the alumina scale and also to reinforce the austenite matrix [73, 78].

After 1000 hours exposure to oxygen-containing molten Pb at 600°C, all samples showing corrosion resistance have preserved the austenite matrix in the alloy bulk. Likewise the precipitation of L1₂-ordered $\text{Ni}_3(\text{Al,Fe})$ phase with f.c.c. structure is observed. This secondary phase known as γ' and found in various Ni-based and Fe-based superalloys, including alumina-forming stainless steels, is reported to provide a strengthening effect, improving the high temperature mechanical properties [71, 72, 75, 77, 78, 85-87, 91].

The study of the corrosion behaviour of Fe-Ni-Cr-Al model alloys, exposed to molten Pb containing 10^{-6} wt. % oxygen, allowed the selection of the appropriate concentration ranges of the alloying elements, at which protective oxide scale is formed and the austenite matrix is preserved. Considering the maximum temperature of 600°C and the specificity of the corrosion issues related to molten Pb and Pb-alloys environments, the design of compatible alumina-forming stainless steels should be based on the following general formula Fe-(20-29)Ni-(15.2-16.5)Cr-(2.3-4.3)Al [wt.%]. At temperatures $\leq 550^\circ\text{C}$, the Cr content may decrease to 14.4 wt.%. To this base formula small amounts of other elements can be added to stabilize the austenite matrix (C, Mn, Cu), increase scale adherence (Y), precipitate the minor phases (Nb, Ti), strengthen the austenite (W, Mo) and its grain boundaries (B). The concentration of the minor elements needs to be correlated with the maximum temperature of the envisaged technological application in order to satisfy in the same time the requirements regarding the properties and the economics.

5. Conclusions

This paper presents the results of the corrosion tests performed in oxygen-containing molten Pb on quaternary Fe-Cr-Al-Ni model alloys, which are designed to display corrosion resistance, while preserving the austenitic structure as the alloy matrix.

The main conclusions are as follows:

(a) From the twelve alloys designed for this study, six have shown corrosion resistance by forming thin and continuous protective oxide scales, during the exposure at 550°C and 600°C for 1000 hours to molten Pb containing 10^{-6} wt.% oxygen.

(b) The constituents of the passivating oxide scales are Cr_2O_3 and Al_2O_3 .

(c) For the passivating scale formation, while preserving the austenitic structure of the alloy matrix, the appropriate concentration ranges for Al, Cr and Ni have been defined based on the experimental results. As a result, a general formula for the backbone of the AFA steels to be designed for applications in Pb and Pb-based alloys environments up to 600°C has been substantiated as follows: Fe-(20-29)Ni-(15.2-16.5)Cr-(2.3-4.3)Al [wt.%]. In case of application temperatures $\leq 550^\circ\text{C}$ the critical Cr content is found at 14.4 wt.%.

(d) A transitional layer, consisting of Fe- and Ni-enriched austenitic matrix and exhibiting randomly distributed intermetallic B2-(Ni,Fe)Al, is formed below the oxide scale up to a depth of two microns.

(e) It was observed that, after 1000h exposure at 600°C to oxygen-containing molten Pb, the microstructure of the bulk alloys consisted in the austenite (γ) and γ' -Ni₃(Al,Fe) phases.

It should be noted that the development of alumina-forming stainless steels for applications which involve long term contact with oxygen-containing HLMs could be a more difficult task when compared to the development of alumina-forming ferritic steels. The difficulty to ensure the required corrosion and mechanical properties resides mainly in the metastability of the austenite, high solubility of Ni in the HLMs, as well as in the increased number of alloying elements, which often produce contradictory effects, and in the microstructure complexity. Therefore, if targeting specific applications in HLMs environments, further careful assessment of minor alloying elements concentrations is required.

Acknowledgment

This work was supported by the Helmholtz program NUSAFE at the Karlsruhe Institute of Technology and has been carried out in the frame of EERA Point Programme of Nuclear Materials, partly funded by the European Commission HORIZON 2020 Framework Programme under grant agreement No. 755269. Hao Shi appreciates the PhD fellowship supported by the China Scholarship Council (CSC No. 201506230151).

Data Availability

The raw/processed data required to reproduce these findings cannot be shared at this time due to technical or time limitations.

The datasets obtained during the current study are available from the corresponding author on reasonable request.

References

- [1] „A technology Roadmap for Generation IV Nuclear Energy Systems“ GIF-002-00 (2002) <https://www.gen-4.org/gif/upload/docs/application/pdf/2013-09/genivroadmap2002.pdf>
- [2] Y. Tian, C.Y. Zhao, A review of solar collectors and thermal energy storage in solar thermal applications, *Appl. Energy*, 104 (2013) 538-553, <https://doi.org/10.1016/j.apenergy.2012.11.051>
- [3] E. González-Roubaud, D. Pérez-Osorio, C. Prieto, Review of commercial thermal energy storage in concentrated solar power plants: Steam vs. molten salts, *Renewable and Sustainable Energy Reviews* 80 (2017) 133-148, <https://doi.org/10.1016/j.rser.2017.05.084>
- [4] Y. Ahn, S.J. Bae, M. Kim, S.K. Cho, S. Baik, J.I. Lee, J. E. Cha, Review of supercritical CO₂ power cycle technology and current status of research and development, *Nuc. Eng. Technol.* 47 (2015) 647-661, <https://doi.org/10.1016/j.net.2015.06.009>
- [5] J.D. Osorio, R. Hovsapien, J.C. Ordonez, Effect of multi-tank thermal energy storage, recuperator effectiveness, and solar receiver conductance on the performance of a concentrated solar supercritical CO₂-based power plant operating under different seasonal conditions, *Energy* 115 (2016) 353–368, <https://doi.org/10.1016/j.energy.2016.08.074>
- [6] Dongke Zhang, *Ultra-Supercritical Coal Power Plants, Materials, Technologies and Optimisation*, Woodhead Publishing Series in Energy, 2013, ISBN 978-0-85709-116-1.
- [7] Z. Su'ud, H. Sekimoto, Design and safety aspect of lead and lead-bismuth cooled long-life small safe fast reactors for various fore configurations, *J. Nucl. Sci. Technol.* 32 (1995) 834–845, <https://doi.org/10.1080/18811248.1995.9731785>
- [8] F. Roelofs, B. de Jager, A. Class, H. Jeanmart, P. Schuurmans, A. Ciampichetti, G. Gerbeth, R. Stieglitz, C. Fazio, European research on HLM thermal hydraulics for ADS applications, *J. Nucl. Mater.* 376 (2008) 401–404, <https://doi.org/10.1016/j.jnucmat.2008.02.014>
- [9] L. Mansani, C. Artioli, M. Schikorr, G. Rimpault, C. Angulo, D. De Bruyn, The European Lead-Cooled EFIT Plant: An Industrial-Scale Accelerator-Driven System for Minor Actinide Transmutation, *Nucl. Technol.* 180 (2012) 241-263, <https://doi.org/10.13182/NT11-96>
- [10] C. D. Bowman, E.D. Arthur, P.W. Lisowski, G.P. Lawrence, et al.: Nuclear energy generation and waste transmutation using an accelerator-driven intense thermal neutron source, *Nuclear Instruments and Methods A* 320 (1992) 336–367, [https://doi.org/10.1016/0168-9002\(92\)90795-6](https://doi.org/10.1016/0168-9002(92)90795-6)
- [11] V. Coen, Lithium-lead eutectic as breeding material in fusion reactors, *J. of Nucl. Mater.* 133-134, (1995) 46-51, [https://doi.org/10.1016/0022-3115\(85\)90110-2](https://doi.org/10.1016/0022-3115(85)90110-2)
- [12] D. Frazer, E. Stergar, C. Cionea, P. Hosemann, Liquid metal as heat transport fluid for thermal solar power applications, *Energy Procedia* 49 (2014) 627-636, <https://doi.org/10.1016/j.egypro.2014.03.068>
- [13] J. Pacio, T. Wetzel, Assessment of liquid metal technology status and research paths for their use as efficient heat transfer fluids in solar central receiver systems, *Sol. Energy* 93 (2013) 11–22, <https://doi.org/10.1016/j.solener.2013.03.025>
- [14] M. Serban, M. A. Lewis, Ch. L. Marshall, R. D. Doctor, Hydrogen production by direct contact pyrolysis of natural gas, *Energy&Fuels* 17 (2003) 705-713, DOI: 10.1021/ef020271q.
- [15] A. Abánades, R. K. Rathnam, T. Geissler, A. Heinzl, K. Mehravaran, G. Müller, M. Plevan, C. Rubbia, D. Salmieri, L. Stoppel, S. Stückrad, A. Weisenburger, H. Wenninger, T. Wetzel, Development of methane decarbonisation based on liquid metal technology for CO₂-free production of hydrogen, *Int. J. Hydrogen Energy*, 41 (2016) 8159–8167, <https://doi.org/10.1016/j.ijhydene.2015.11.164>
- [16] H. Kim, D. Boysen, J. Newhouse, B. Spatocco, B. Chung, P. Burke, D. Bradwell, K. Jiang, A. Tomaszowska, K. Wang, W. Wei, L. Ortiz, S. Barriga, S. PoizeauD. Sadoway, Liquid metal batteries: Past, present, and future, *Chem. Rev.*, 113 (2013) 2075-2099, DOI: 10.1021/cr300205k.
- [17] K. Wang, K. Jiang, B. Chung, T. Ouchi, P. J. Burke, D. A. Boysen, D. J. Bradwell, H. Kim, U. Muecke, D. R. Sadoway, Lithium–antimony–lead liquid metal battery for grid-level energy storage, *Nature* 514 (2014) 348–350, doi: 10.1038/nature13700.

- [18] R.C. Asher, D. Davies, S.A. Beetham, Some observations on the compatibility of structural materials with molten lead, *Corros. Sci.* 17 (1977) 545-557, [https://doi.org/10.1016/S0010-938X\(77\)80001-2](https://doi.org/10.1016/S0010-938X(77)80001-2)
- [19] Handbook on Lead–Bismuth Eutectic Alloy and Lead Properties, Material Compatibility, Thermal–Hydraulics and Technologies, AEN/NEA Nuclear Energy Agency, OECD, Nuclear Science, 2015 NEA No.7268, (accessed 26/04/2019) <https://www.oecd-nea.org/science/pubs/2015/7268-lead-bismuth-2015.pdf>
- [20] V.S. Rao, J. Lim, I.S. Hwang, L.K. Singhal, Characterization of oxide scales grown on 316L stainless steels in liquid lead–bismuth eutectic, *Corros. Sci.* 63 (2012) 113-118, <https://doi.org/10.1016/j.corsci.2012.05.016>
- [21] Y. Kurata, M. Futakawa, S. Saito, Comparison of the corrosion behavior of austenitic and ferritic/martensitic steels exposed to static liquid Pb–Bi at 450 and 550 °C, *J. Nucl. Mater.* 343 (2005) 333-340, <https://doi.org/10.1016/j.jnucmat.2004.07.064>
- [22] A.K. Rivai, M. Takahashi, Corrosion characteristics of materials in Pb–Bi under transient temperature conditions, *J. Nucl. Mater.* 398 (2010) 139-145, <https://doi.org/10.1016/j.jnucmat.2009.10.024>
- [23] E. Yamaki, K. Ginestar, L. Martinelli, Dissolution mechanism of 316L in lead–bismuth eutectic at 500 °C, *Corros. Sci.* 53 (2011) 3075-3085, <https://doi.org/10.1016/j.corsci.2011.05.031>
- [24] J.S. Zhang, A review of steel corrosion by liquid lead and lead–bismuth, *Corros. Sci.* 51 (2009) 1207-1227, <https://doi.org/10.1016/j.corsci.2009.03.013>
- [25] D. Sapundjiev, S. Van Dyck, W. Bogaerts, Liquid metal corrosion of T91 and A316L materials in Pb–Bi eutectic at temperatures 400–600 °C, *Corros. Sci.* 48/3 (2006) 577-594, <https://doi.org/10.1016/j.corsci.2005.04.001>
- [26] C. Schroer, O. Wedemeyer, J. Novotny, A. Skrypnik, J. Konys, Selective leaching of nickel and chromium from Type 316 austenitic steel in oxygen-containing lead–bismuth eutectic (LBE), *Corros. Sci.* 84 (2014) 113-124, <https://doi.org/10.1016/j.corsci.2014.03.016>
- [27] A. Weisenburger, C. Schroer, A. Jianu, A. Heinzl, J. Konys, H. Steiner, G. Müller, C. Fazio, A. Gessi, S. Babayan, A. Kobzova, L. Martinelli, K. Ginestar, F. Balbaud-Célrier, F.J. Martín-Muñoz, L. Soler Crespo, Long term corrosion on T91 and AISI 316L steel in flowing lead alloy and corrosion protection barrier development: Experiments and models, *J. Nucl. Mater.* 415/3 (2011) 260-269, <https://doi.org/10.1016/j.jnucmat.2011.04.028>
- [28] J.R. Weeks, Lead, bismuth, tin and their alloys as nuclear coolant, *Nucl. Eng. Design* 15 (1971) 363-372, DOI: 10.1016/0029-5493(71)90075-6.
- [29] G. Muller, G. Schumacher, and F. Zimmermann, Investigation on Oxygen Controlled Liquid Lead Corrosion of Surface Treated Steels, *J. Nucl. Mater.* 278 (2000) 85-95, [https://doi.org/10.1016/S0022-3115\(99\)00211-1](https://doi.org/10.1016/S0022-3115(99)00211-1)
- [30] A. Weisenburger, G. Müller, A. Heinzl, A. Jianu, H. Muscher, M. Kieser, Corrosion, Al containing corrosion barriers and mechanical properties of steels foreseen as structural materials in liquid lead alloy cooled nuclear systems, *Nucl. Eng. & Design* 241/5 (2011) 1329-1334, <https://doi.org/10.1016/j.nucengdes.2010.08.005>
- [31] V. Tsisar, C. Schroer, O. Wedemeyer, A. Skrypnik, J. Konys, Long-term corrosion of austenitic steels in flowing LBE at 400°C and 10^{-7} mass% dissolved oxygen in comparison with 450 and 550°C, *J. Nucl. Mater.* 468 (2016) 305-312, <https://doi.org/10.1016/j.jnucmat.2015.09.027>
- [32] L. Martinelli, T. Dufrenoy, K. Jaakou, A. Rusanov, F. Balbaud-Célrier, High temperature oxidation of Fe–9Cr–1Mo steel in stagnant liquid lead–bismuth at several temperatures and for different lead contents in the liquid alloy, *J. Nucl. Mater.* 376 (2008) 282-288, <https://doi.org/10.1016/j.jnucmat.2008.02.006>
- [33] G. Müller, A. Heinzl, J. Konys, G. Schumacher, A. Weisenburger, F. Zimmermann, V. Engelko, A. Rusanov, V. Markov, Results of steel corrosion tests in flowing liquid Pb/Bi at 420–600 °C after 2000 h, *J. Nucl. Mater.* 301 (2002) 40-46, [https://doi.org/10.1016/S0022-3115\(01\)00725-5](https://doi.org/10.1016/S0022-3115(01)00725-5)
- [34] T.B. Massalski, (Ed.), *Binary Phase Diagrams*, ASM Int., Materials Park, OH, 1990.
- [35] O. Madelung (Ed.), *Landolt–Bornstein New Series IV*, vol.5, Springer, Berlin, 1995.

- [36] R. Ballinger, J. Lim An overview of corrosion issues for the design and operation of high temperature lead- and lead-bismuth-cooled reactor systems, *Nucl. Techn.* 147/3 (2004) 418-435, <https://doi.org/10.13182/NT04-A3540>
- [37] B.A. Shmatko, A.E. Rusanov, Oxide protection of materials in melts of lead and bismuth *Mater. Sci.* 36 (2000) 689-700, <https://doi.org/10.1023/A:1011307907891>
- [38] B.F. Gromov, Yu.I. Orlov, P.N. Martynov, K.D. Ivanov, V.A. Gulevski, Physical-chemical principles of lead-bismuth coolant technology in: H.U. Borgstedt, G. Frees (Eds.), *Liquid Metal Systems*, Plenum, New York (1995) 339-343, https://doi.org/10.1007/978-1-4615-1977-5_37
- [39] M. Roy, L. Martinelli, K. Ginestar, J. Favregeon, G. Moulin, Dissolution and oxidation behaviour of various austenitic steels and Ni rich alloys in lead-bismuth eutectic at 520 °C, *J. Nucl. Mater.* 468 (2016) 153-163, <https://doi.org/10.1016/j.jnucmat.2015.11.005>
- [40] A. Jianu, G. Mueller, A. Weisenburger, A. Heinzl, C. Fazio, V.G. Markov, A.D. Kashtanov, Creep-to-rupture tests of T91 steel in flowing Pb–Bi eutectic melt at 550 °C, *J. Nucl. Mater.* 394/1 (2009) 102-108, <https://doi.org/10.1016/j.jnucmat.2009.08.013>
- [41] A. Weisenburger, A. Jianu, W. An, R. Fetzner, M. DelGiacco, A. Heinzl, G. Müller, V.G. Markov, A.D. Kashtanov, Creep, creep-rupture tests of Al-surface-alloyed T91 steel in liquid lead bismuth at 500 and 550 °C, *J. Nucl. Mater.* 431/1-3 (2012) 77-84, <https://doi.org/10.1016/j.jnucmat.2011.11.027>
- [42] H.U. Borgstedt, H. Glasbrenner, Development of a direct insulation layer for a self-cooled liquid metal fusion reactor blanket, *Fusion Eng. Des.* 27 (1995) 659-662, [https://doi.org/10.1016/0920-3796\(95\)90181-7](https://doi.org/10.1016/0920-3796(95)90181-7)
- [43] G.S. Yachmenyov, A.Ye. Rusanov, B.F. Gromov, Yu.S. Belomytsev, N.S. Skvortsov, A.P. Demishonkov, Proceedings of Heavy Liquid Metal Coolants in Nuclear Technology, HLMC'98, 5–9 October 1998, Obninsk, Russia, 1999, 133-139.
- [44] Y. Kurata, M. Futakawa, Excellent corrosion resistance of 18Cr–20Ni–5Si steel in liquid Pb–Bi. *J. Nucl. Mater.* 325 (2004) 217-222, <https://doi.org/10.1016/j.jnucmat.2003.12.009>
- [45] V. Gorynin, G.P. Karzov, V.G. Markov, and V.A. Yakovlev, Structural materials for atomic reactors with liquid metal heat-transfer agents in the form of lead or lead–Bismuth alloy, *Met. Sci. Heat Treat.* 41 (1999) 384-391, <https://doi.org/10.1007/BF02469876>
- [46] M. Kondo, M. Takahashi, Corrosion resistance of Si- and Al-rich steels in flowing lead–bismuth, *J. Nucl. Mater.* 356 (2006) 203-212, <https://doi.org/10.1016/j.jnucmat.2006.05.019>
- [47] M. Ph. Short, R.G. Ballinger, A Functionally Graded Composite for Service in High-Temperature Lead- and Lead-Bismuth–Cooled Nuclear Reactors—I: Design, *Nucl. Technol.* 177 (2012) 366-381, <https://doi.org/10.13182/NT12-A13481>
- [48] P. Hosemann, H.T. Thau, A.L. Johnson, S.A. Maloy, N. Li, Corrosion of ODS steels in lead–bismuth eutectic, *J. Nucl. Mater.* 373 (2008) 246-253, <https://doi.org/10.1016/j.jnucmat.2007.05.049>
- [49] J. Lim, H.O. Nam, I.S. Hwang, J.H. Kim, A study of early corrosion behaviors of FeCrAl alloys in liquid lead–bismuth eutectic environments, *J. Nucl. Mater.* 407 (2010) 205-210, <https://doi.org/10.1016/j.jnucmat.2010.10.018>
- [50] J. Ejenstam, M. Thuvander, P. Olsson, F. Rave, P. Szakalos, Oxidation studies of Fe10CrAl-RE alloys exposed to Pb at 550 C for 10,000 h, *J. Nucl. Mater.* 443 (2013) 161-170, <https://doi.org/10.1016/j.jnucmat.2013.07.023>
- [51] R. Gao, L.L. Xia, T. Zhang, X.P. Wang, Q.F. Fang, C.S. Liu, Oxidation resistance in LBE and air and tensile properties of ODS ferritic steels containing Al/Zr elements, *J. Nucl. Mater.* 455 (2014) 407-411, <https://doi.org/10.1016/j.jnucmat.2014.07.028>
- [52] M. Del Giacco, A. Weisenburger, A. Jianu, F. Lang, G. Mueller, Influence of composition and microstructure on the corrosion behavior of different Fe–Cr–Al alloys in molten LBE, *J. Nucl. Mater.* 421 (2012) 39-46, <https://doi.org/10.1016/j.jnucmat.2011.11.049>
- [53] G. Zhang, Z. Zhou, K. Mo, P. Wang, Y. Miao, S. Li, M. Wang, X. Liu, M. Gong, J. Almer, J. Stubbins, The microstructure and mechanical properties of Al-containing 9Cr ODS ferritic alloy, *J. Alloys and Comp.* 648 (2015) 223-228, <https://doi.org/10.1016/j.jallcom.2015.06.214>
- [54] S. Takaya, T. Furukawa, K. Aoto, G. Müller, A. Weisenburger, A. Heinzl, M. Inoue, T. Okuda, F. Abe, S. Ohnuki, T. Fujisawa, A. Kimura, Corrosion behavior of Al-alloying high Cr-ODS steels in lead–bismuth eutectic, *J. Nucl. Mater.* 386-388 (2009) 507-510, <https://doi.org/10.1016/j.jnucmat.2008.12.155>

- [55] K. Unocic, D. Hoelzer, Evaluation of Pb-17Li compatibility of ODS Fe-12Cr-5Al alloys, *J. Nucl. Mater.* 479 (2016) 357-364, <https://doi.org/10.1016/j.jnucmat.2016.07.017>
- [56] C. Cionea, M.D. Abad, Y. Aussat, D. Frazer, A.J. Gubser, P. Hosemann, Oxide scale formation on 316L and FeCrAl steels exposed to oxygen controlled static LBE at temperatures up to 800 °C, *Solar energy materials @ solar cells* 144 (2016) 235-246, <https://doi.org/10.1016/j.solmat.2015.09.007>
- [57] S. Takaya, T. Furukawa, G. Müller, A. Heinzl, A. Jianu, A. Weisenburger, K. Aoto, M. Inoue, T. Okuda, F. Abe, S. Ohnuki, T. Fujisawa, A. Kimura, Al-containing ODS steels with improved corrosion resistance to liquid lead–bismuth, *J. Nucl. Mater.* 428 (2012) 125-130, <https://doi.org/10.1016/j.jnucmat.2011.06.046>
- [58] M.P. Popovic, Y. Yang, A. M. Bolind, V.B. Ozdol, D.L. Olmsted, M. Asta, P. Hosemann, Transmission Electron Microscopy (TEM) Study of the Oxide Layers Formed on Fe-12Cr-4Al Ferritic Alloy in an Oxygenated Pb-Bi Environment at 800°C, *JOM* 70 (2018) 1471-1477, <https://doi.org/10.1007/s11837-018-2951-8>
- [59] A. Jianu, R. Fetzer, A. Weisenburger, S. Doyle, M. Bruns, A. Heinzl, P. Hosemann, G. Mueller, Stability domain of alumina thermally grown on FeCrAl-based model alloys and modified surface layers exposed to oxygen-containing molten Pb, *J. Nucl. Mater.* 2016, 470, 68-75, <https://doi.org/10.1016/j.jnucmat.2015.12.009>
- [60] J. Lim, I.S. Hwang, J. H. Kim, Design of alumina forming FeCrAl steels for lead or lead–bismuth cooled fast reactors, *J. Nucl. Mater.* 441 (2013) 650-660, <https://doi.org/10.1016/j.jnucmat.2012.04.006>
- [61] M.N. Gushev, K.G. Field, Y. Yamamoto, Design, properties, and weldability of advanced oxidation-resistant FeCrAl alloys, *Materials & Design* 129 (2017) 227-238, <https://doi.org/10.1016/j.matdes.2017.05.009>
- [62] A. Weisenburger, A. Heinzl, G. Mueller, H. Muscher, A. Rusanov, T91 cladding tubes with and without modified FeCrAlY coatings exposed in LBE at different flow, stress and temperature conditions, *J. Nucl. Mater.* 376/3 (2008) 274-281, <https://doi.org/10.1016/j.jnucmat.2008.02.026>
- [63] G. Müller, A. Heinzl, J. Konys, G. Schumacher, A. Weisenburger, F. Zimmermann, V. Engelko, A. Rusanov, V. Markov, Behavior of steels in flowing liquid PbBi eutectic alloy at 420–600 °C after 4000–7200 h, *J. Nucl. Mater.* 335 (2004) 163-168, <https://doi.org/10.1016/j.jnucmat.2004.07.010>
- [64] V. Engelko, G. Mueller, A. Rusanov, V. Markov, K. Tkachenkov, A. Weisenburger, A. Kashtanov, A. Chikiryaka, A. Jianu, Surface modification/alloying using intense pulsed electron beam as a tool for improving the corrosion resistance of steels exposed to heavy liquid metals, *J. Nucl. Mater.* 415/3 (2011) 270-275, <https://doi.org/10.1016/j.jnucmat.2011.04.030>
- [65] A. Weisenburger, G. Rizzi, A. Scrivani, G. Mueller, J.R. Nicholls Pulsed electron beam treatment of MCrAlY bondcoats for EB-PVD TBC systems part 1 of 2: Coating production, *Surface and Coatings Technology*, 202/4-7 (2007) 704-708, <https://doi.org/10.1016/j.surfcoat.2007.07.022>
- [66] R. Fetzer, A. Weisenburger, A. Jianu, G. Müller, Oxide scale formation of modified FeCrAl coatings exposed to liquid lead, *Corros. Sci.* 55 (2012) 213-218, <https://doi.org/10.1016/j.corsci.2011.10.019>
- [67] T. Auger, G. Lorang, Liquid metal embrittlement susceptibility of T91 steel by lead–bismuth, *Scr. Mater.* 52 (2005) 323-328, <https://doi.org/10.1016/j.scriptamat.2005.02.027>
- [68] F. Ersoy, S. Gavrilo, K. Verbeken, Investigating liquid-metal embrittlement of T91 steel by fracture toughness tests, *J. Nucl. Mater.* 472 (2016) 171-177, <https://doi.org/10.1016/j.jnucmat.2015.12.019>
- [69] Y. Yamamoto, M.P. Brady, Z.P. Lu, P.J. Maziasz, C.T. Liu, B.A. Pint, K.L. More, H.M. Meyer, E.A. Payzant, Creep-resistant Al₂O₃-forming austenitic stainless steels, *Science* 316 (2007) 433-436, DOI: 10.1126/science.1137711.
- [70] Y. Yamamoto, M.P. Brady, Z.P. Lu, C.T. Liu, M. Takeyama, P.J. Maziasz, B.A. Pint, Alumina-forming austenitic stainless steels strengthened by Laves phase and MC carbide precipitates, *Metall. Mater. Trans. A* 38A (2007) 2737-2746, <https://doi.org/10.1007/s11661-007-9319-y>
- [71] Y. Yamamoto, M.P. Brady, M.L. Santella, H. Bei, P.J. Maziasz, and B.A. Pint, Overview of strategies for high-temperature creep and oxidation resistance of alumina-forming austenitic stainless steels, *Metall. Mater. Trans. A* 42A (2011) 922-931, <https://doi.org/10.1007/s11661-010-0295-2>
- [72] Y. Yamamoto, M. P. Brady, G. Muralidharan, B. A. Pint, P. J. Maziasz, D. Shin, B. Shassere, S. S. Babu, C.-H. Kuo, Development of Creep-Resistant, Alumina-Forming Ferrous Alloys for High-

Temperature Structural Use, Proceedings of the ASME 2018 Symposium on Elevated Temperature Application, of Materials for Fossil, Nuclear, and Petrochemical Industries, ETAM2018, ISBN: 978-0-7918-4076-4 <http://proceedings.asmedigitalcollection.asme.org/proceeding.aspx?articleid=2681231> doi:10.1115/ETAM2018-6727.

[73] Y. Yamamoto, M.L. Santanella, M.P. Brady, H. Bei, P.J. Maziasz, Effect of alloying additions on phase equilibria and creep resistance of alumina-forming austenitic stainless steels, *Metall. Mater. Trans. A* 40A (2009) 1868-1880, <https://doi.org/10.1007/s11661-009-9886-1>

[74] D.Q. Zhou, W.X. Zhao, H.H. Mao, Y.X. Hu, X.Q. Xu, X.Y. Sun, Z.P. Lu, Precipitate characteristics and their effects on the high-temperature creep resistance of alumina-forming austenitic stainless steels, *Materials Science and Engineering: A* 622 (2015) 91-100, <https://doi.org/10.1016/j.msea.2014.11.013>

[75] G. Trotter, B. Hu, A. Y. Sun, R. Harder, M.K. Miller, L. Yao, I. Baker, Precipitation kinetics during aging of an alumina-forming austenitic stainless steel, *Materials Science and Engineering: A* 667 (2016) 147-155, <https://doi.org/10.1016/j.msea.2016.04.081>

[76] B. Hu, I. Baker, High temperature deformation of Laves phase precipitates in alumina-forming austenitic stainless steels, *Materials Letters* 195 (2017) 108-111, <https://doi.org/10.1016/j.matlet.2017.02.086>

[77] J. Moon, T.-H. Lee, Y.-U. Heo, Y.-S. Han, J.-Y. Kang, H.-Y. Ha, D.-W. Suh, Precipitation sequence and its effect on age hardening of alumina-forming austenitic stainless steel, *Materials Science and Engineering: A* 645 (2015) 72-81, <https://doi.org/10.1016/j.msea.2015.08.005>

[78] M.P. Brady, Y. Yamamoto, M.L. Santella, and L.R. Walker, Composition, Microstructure, and Water Vapor Effects on Internal/External Oxidation of Alumina-Forming Austenitic Stainless Steels, *Oxid. Met.* 72/5-6 (2009) 311-333, <https://doi.org/10.1007/s11085-009-9161-2>

[79] X.Q. Xu, X.F. Zhang, G.L. Chen, Z.P. Lu, Improvement of high-temperature oxidation resistance and strength in alumina-forming austenitic stainless steels, *Mater. Lett.* 65 (2011) 3285-3288, <https://doi.org/10.1016/j.matlet.2011.07.021>

[80] X.Q. Xu, X.F. Zhang, X.Y. Sun, Z.P. Lu, Roles of Manganese in the High-temperature Oxidation Resistance of Alumina-forming Austenitic Steels at above 800 °C, *Oxid. Metals* 78 (2012) 349-362, <https://doi.org/10.1007/s11085-012-9311-9>

[81] X.Q. Xu, X.F. Zhang, X.Y. Sun, Z.P. Lu, Effects of silicon additions on the oxide scale formation of an alumina-forming austenitic alloy, *Corrosion Sci.* 65 (2012) 317-321, <https://doi.org/10.1016/j.corsci.2012.08.039>

[82] M.P. Brady, K. Unocic, M. Lance, M. Santella, Y. Yamamoto, L. Walker, Increasing the Upper Temperature Oxidation Limit of Alumina Forming Austenitic Stainless Steels in Air with Water Vapor, *Oxid. Metals* 75 (2011) 337-357, <https://doi.org/10.1007/s11085-011-9237-7>

[83] W.G. Zhao, Y. Wu, S.G. Jiang, H. Wang, X.G. Liu, Z.G. Lu, Micro-alloying Effects of Yttrium on Recrystallization Behavior of an Alumina-forming Austenitic Stainless Steel, *J. Iron and Steel Res.* 23/6 (2016) 553-558, [https://doi.org/10.1016/S1006-706X\(16\)30087-5](https://doi.org/10.1016/S1006-706X(16)30087-5)

[84] M.H. Jang, J.Y. Kang, J. H. Jang, T.H. Lee, C. Lee, Improved creep strength of alumina-forming austenitic heat-resistant steels through W addition, *Mater. Sci. and Eng. A* 696 (2017) 70-79, <https://doi.org/10.1016/j.msea.2017.04.062>

[85] B. Zhao, J. Fan, Z. Chen, X. Dong, F. Sun, L. Zhang, Evolution of precipitates in a Cu-containing alumina-forming austenitic steel after short-term mechanical tests, *Materials Characterization* 125 (2017) 37-45, <https://doi.org/10.1016/j.matchar.2017.01.023>

[86] B. Hu, G. Trotter, Z. Wang, S. Chen, Z. Cai, I. Baker, Effect of boron and carbon addition on microstructure and mechanical properties of the aged gamma-prime strengthened alumina-forming austenitic alloys, *Intermetallics* 90 (2017) 36-49, <https://doi.org/10.1016/j.intermet.2017.06.011>

[87] B. Zhao, J. Fan, Y. Liu, L. Zhao, X. Dong, F. Sun, L. Zhang, Formation of L1₂-ordered precipitation in an alumina-forming austenitic stainless steel via Cu addition and its contribution to creep/rupture resistance, *Scripta Materialia* 109 (2015) 64-67, <https://doi.org/10.1016/j.scriptamat.2015.07.019>

[88] P.J. Maziasz, Development of creep-resistant and oxidation-resistant austenitic stainless steels for high temperature applications, *JOM*, 70/1 (2018) 66-75, <https://doi.org/10.1007/s11837-017-2642-x>

- [89] J. Romu, T. Sarikka, M. Heikkilä, I. Virkkunen, H. Hänninen, Early stage oxidation behaviour of Al- and Si-alloyed stainless steels as well as Ni-based alloys in air at elevated temperatures, *Mater. And Corrosion* 69 (2018) 690-702, <https://doi.org/10.1002/maco.201709836>
- [90] X. Guo, K. Chen, W. Gao, Z. Shen, L. Zhang, Corrosion behaviour of alumina-forming and oxide dispersion strengthened austenitic 316 stainless steel in supercritical water, *Corr. Sci.* 138 (2018) 297-306, <https://doi.org/10.1016/j.corsci.2018.04.026>
- [91] M.P. Brady, J. Magee, Y. Yamamoto, D. Helmick, L. Wang, Co-optimization of wrought alumina-forming austenitic stainless steel composition ranges for high-temperature creep and oxidation/corrosion resistance, *Mater. Sci. and Eng. A* 590 (2014) 101-115, <https://doi.org/10.1016/j.msea.2013.10.014>
- [92] L.F. He, P. Roman, B. Leng, K. Sridharan, M. Anderson, T. Allen, Corrosion behavior of an alumina forming austenitic steel exposed to supercritical carbon dioxide, *Corr. Sci.* 82 (2014) 67-76, <https://doi.org/10.1016/j.corsci.2013.12.023>
- [93] Y.F. Yan, X.Q. Xu, D.Q. Zhou, H. Wang, Y. Wu, X.J. Liu, Z.P. Lu, Hot corrosion behaviour and its mechanism of a new alumina-forming austenitic stainless steel in molten sodium sulphate, *Corr. Sci.* 77 (2013) 202-209, <https://doi.org/10.1016/j.corsci.2013.08.003>
- [94] A. Rouaix-Vande Put, K. Unocic, M.P. Brady, B.A. Pint, Performance of chromia- and alumina-forming Fe- And Ni-base alloys exposed to metal dusting environments: the effect of water vapor and temperature, *Corr. Sci.* 82 (2015) 58-68, <https://doi.org/10.1016/j.corsci.2014.11.022>
- [95] J. Ejenstam, P. Szakalos, Long term corrosion resistance of alumina forming austenitic stainless steels in liquid lead, *J. Nucl. Mater.* 461 (2015) 164-170, <https://doi.org/10.1016/j.jnucmat.2015.03.011>
- [96] A.L. Schaeffler, Constitution diagram for stainless steel weld metal, *Met. Prog.* 56 (1949) 680-680B.
- [97] R.H. Espy, Weldability of nitrogen-strengthened stainless steels, *Weld. J.* 61 (1982) S149-S156.
- [98] F.H. Stott, G.C. Wood, J. Stringer, The influence of alloying elements on the development and maintenance of protective scales, *Oxid. Met.* 44 1/2 (1995) 113-145, <https://doi.org/10.1007/BF01046725>
- [99] C. Wagner, Passivity and inhibition during the oxidation of metals at elevated temperatures, *Corros. Sci.* 5 (1965) 751-764, [https://doi.org/10.1016/S0010-938X\(65\)80003-8](https://doi.org/10.1016/S0010-938X(65)80003-8)
- [100] M. A. Payne, J. B. Miller, A. J. Gellmann, High-throughput screening across quaternary alloy composition space: oxidation of $(\text{Al}_x\text{Fe}_y\text{Ni}_{1-x-y})_{-0.8}\text{Cr}_{-0.2}$, *ACS Comb. Sci.* 18 (2016) 559-568, DOI: 10.1021/acscombsci.6b00047.
- [101] R. Peraldi, B.A. Pint, Effect of Cr and Ni contents on the oxidation behaviour of ferritic and austenitic model alloys in air with water vapor, *Oxid. Met.* 61 (2004) 463-483, <https://doi.org/10.1023/B:OXID.0000032334.75463.da>
- [102] J. Emo, Ph. Maugis, A. Perlade, Austenite growth and stability in medium Mn, medium Al, Fe-C-Mn-Al steels, *Comp. Mat. Sci.* 125 (2016) 206-217, <https://doi.org/10.1016/j.commatsci.2016.08.041>
- [103] P. Zhao, H. Zhao, J. Hu, H. Zhang, H. Gao, Q. Chen, Crystal structure and properties of Al_2O_3 - Cr_2O_3 solid solution with different Cr_2O_3 contents, *Ceram. Inter.* 44 (2018) 1356-1361, <https://doi.org/10.1016/j.ceramint.2017.08.195>
- [104] E. Charalampopoulou, R. Delville, M. Verwerft, K. Lambrinou, D. Schryvers, Transmission electron microscopy study of complex oxide scales on DIN 1.4970, steel exposed to liquid Pb-Bi eutectic, *Corr. Sci.* 147 (2019) 22-31 <https://doi.org/10.1016/j.corsci.2018.10.018>
- [105] P. Hosemann, D. Frazer, E. Stergar, K. Lambrinou, Twin boundary-accelerated ferritization of austenite stainless steels in liquid lead-bismuth eutectic. *Scr. Mater.* 118 (2016) 37-40 <http://dx.doi.org/10.1016/j.scriptamat.2016.02.029>
- [106] K. Lambrinou, E. Charalampopoulou, T. van der Donck, R. Delville, D. Schryvers, Dissolution corrosion of 316L austenitic stainless steels in contact with static liquid lead-bismuth eutectic (LBE) at 500°C. *J. Nucl. Mater.* 490 (2017) 9-27 <http://dx.doi.org/10.1016/j.jnucmat.2017.04.004>

- [107] O. Klok, K. Lambrinou, S. Gavrilov, E. Stergar, J. Lim, T. van der Donck, W. van Renterghem, I. de Graeve, Effect of deformation twinning on dissolution corrosion of 316L stainless steels in contact with Static liquid lead-bismuth eutectic (LBE) at 500°C. *J. Nucl. Mater.* 510 (2018) 556-567.
<https://doi.org/10.1016/j.jnucmat.2018.08.030>
- [108] O. Klok, K. Lambrinou, S. Gavrilov, E. Stergar, T. van der Donck, Sh. Huang, B. Tunca, I. de Graeve, Influence of plastic deformation on dissolution corrosion of type 316L austenitic stainless steel in static, oxygen-poor liquid lead-bismuth eutectic at 500°C, *Corrosion* 73 (2018) 1078-1090.
<https://doi.org/10.5006/2400>
- [109] P. Hosemann, R. Dickerson, P. Dickerson, N. Li, S.A. Maloy, Transmission electron microscopy (TEM) on oxide layers formed on D9 stainless steel in lead bismuth eutectic (LBE), *Corr. Sci.* 66 (2013) 196-202
<http://dx.doi.org/j.corsci.2012.09.019>
- [110] K. Lambrinou, V. Koch, G. Coen, J. van den Bosch, C. Schroer, Corrosion scales on various steels after exposure to liquid lead-bismuth eutectic, *J. Nucl. Mater.* 450 (2014) 244-255.
<http://dx.doi.org/10.106/j.jnucmat.2013.09.034>
- [111] H. von Kantzow, Fire-resistant alloy with high electric resistance, US patent no. 1717284 (1929)
- [112] Y. Niu, S. Wang, F. Gao, Z.G. Zhang, F. Gesmundo, The nature of the third-element effect in the oxidation of Fe-xCr-3at% Al alloys in 1atm O₂ at 1000°C, *Corr. Sci.* 50 (2008) 345-356
<https://doi.org/10.1016/j.corsci.2007.06.019>
- [113] H. Götlind, F. Liu, J.-E. Svensson, M. Halvarsson, L.G. Johansson, The effect of water vapour on the initial stages of oxidation of FeCrAl alloy Kanthal AF at 900°C, *Oxid. Met.* 67 (2007) 251-266
<https://doi.org/10.1007/s11085-007-9055-0>
- [114] D. Giuranno, F. Gnecco, E. Ricci, R. Novakovic, Surface tension and wetting behaviour of molten Bi-Pb alloys, *Intermetallics*, 11 (2003) 1313-1317 doi:10.1016/S0966-9795(03)00173-0
- [115] N. Eustathopoulos, Wetting by liquid metals - applications in materials processing; the contribution of the Grenoble group, *Metals* 5 (2015) 350-370 doi:10.3390/met5010350
- [116] C. Schroer, Guidelines for Corrosion Testing in Liquid Metals (Pb, LBE), MATTER project, deliverable report D3.4, (2011-2015), 26 (accessed 26/04/2019)
[http://www.eera-jpnm.eu/filesarer/documents/Euratom Projects/Past%20projects/MATTER%20public%20deliverables/Deliverable%20D3.4%20MATTER.pdf](http://www.eera-jpnm.eu/filesarer/documents/Euratom%20Projects/Past%20projects/MATTER%20public%20deliverables/Deliverable%20D3.4%20MATTER.pdf)
- [117] C. Fazio, I. Ricapito, G. Scaddozo, G. Benamati, Corrosion behavior of steels and refractory metals and tensile features of steels exposed to flowing PbBi in the LECOR loop, *J. Nucl. Mater.* 318 (2003) 325-332 doi:10.1016/S0022-3115(03)00009-6